ABSTRACT

MARASHI, CAMERON SEPEHR Investigation of Attenuation of Ultrasonic Modes in Optical Fibers and Acoustic Couplers for Sensing Applications (Under the direction of Dr. Kara Peters and Dr. Phillip Bradford).

Fiber Bragg gratings (FBGs) are currently a popular sensor choice for detecting acoustic vibrations. In the field of structural health monitoring (SHM) FBGs are used to detect ultrasonic Lamb waves in structures. However, the FBG interrogation techniques required to make ultrasonic sensing possible also inhibit the ability to multiplex individual FBG signals. Furthermore, modifying already existing sensing systems is a challenge at present when the FBGs are directly fixed to the structure. Recently, research has explored propagating longitudinal modes along optical fibers for SHM purposes. This technique may offer the ability to mitigate some of the limitations currently associated with FBG based SHM. Through the development of a passive acoustic signal coupling device, the propagating mode can also be guided and transferred between separate waveguides at will.

Using cyanoacrylate (CA) based acoustic coupling devices for SHM has been successfully demonstrated in the past. However, in these cases the coupler's performance was limited by large insertion losses and input reflections. A major hindrance to practical application since widely used SHM techniques, such as the pitch catch method, require the sensor to receive high amplitude signals.

This dissertation explores methods for preserving acoustic signals in coupled fiber networks. In the first experiment, the capabilities of a molded CA coupler with defined geometry are thoroughly investigated. In this experiment signal propagation was mapped and the performance and stability of the coupler was quantified. The results show that performance was hindered by material losses and an impedance miss match introduced by the CA. The next

experiment measured the attenuation along silica waveguides of various diameters, since mode leakage is prevalent in longitudinal modes. A laser Doppler vibrometry (LDV) based method for measuring the attenuation along a waveguide was developed. In this experiment we demonstrated that the overall attenuation decreased as the diameter of the waveguide increased. Highlighting the diameter dependent mode leakage is one of the largest contributors to overall acoustic attenuation along a single mode optical fiber (SMOF). In the last chapter, a novel flow coating fabrication technique was implemented to address the limitations observed in previous coupler experiments. Through a CA-acetone solution, capillary forces can distribute the solution between the fibers. Producing uniform couplers with minimal CA deposited. Couplers fabricated with technique displayed higher levels of signal transfer and significantly lower levels of signal loss compared to the molded counterpart. The length of the fabricated coupler was then steadily decreased while the behavior was observed. The signal power was evenly split across the outputs of the coupler regardless of the length.

The results of these experiments show that signal loss through a coupled fiber network can be easily and effectively reduced with slight modifications to the network. It was also observed that signal transfer through an acoustic coupler for optical fibers is not strictly governed by coupled mode theory between parallel waveguides.

Investigation of Attenuation of Ultrasonic Modes in Optical Fibers and Acoustic Couplers for Sensing Applications

by
Cameron Sepehr Marashi

A dissertation submitted to the Graduate Faculty of
North Carolina State University
in partial fulfillment of the
requirements for the degree of
Doctor of Philosophy

Mechanical Engineer

Raleigh, North Carolina
2024

APPROVED BY:

Kara Peters Committee Chair	Philip Bradford Committee Co-Chair
Xiaoning Jiang	Mohammed Zikry
Fuh-Gwo Yuan	

DEDICATION

The work contained in this document is dedicated to my parents Armita and Amir Marashi, my grandmother Shahin, my aunt Homa, and my sister Sara. All of whom pulled the best out of me when I didn't see my potential. None of my accomplishments would have been possible without the many sacrifices my family made for me. I would be nothing without them or their support.

BIOGRAPHY

Cameron Marashi was born on August 13th, 1996, in Mankato, Minnesota. The child of two Iranian immigrants. He attended the University of North Carolina at Charlotte earning his Bachelor of Science degree in Mechanical Engineering in December of 2018. Not being one to wait around he joined the M.S/Ph.D. combined program in Mechanical and Aerospace Engineering at North Carolina State University in January of 2019. Since then, he has worked under Dr. Kara Peters as a graduate student in the Smart Composite Laboratory.

ACKNOWLEDGMENTS

First and foremost, I would like to thank Dr. Kara Peters for her invaluable guidance and dedication as my advisor. Thanks to her I have developed so much as a scientist and researcher in the last 5 years. My appreciation for all her help cannot be overstated.

I would like to extend my appreciation for the members of my committee Dr. Bradford, Dr. Zikry, Dr. Jiang, Dr. Yuan, and Dr. Yang. I thoroughly enjoyed my time in each of your classes and I am grateful I had the opportunity to share my research with you.

I would also like to thank Luna, Dr. Hannah Javidi, and Jenise Fernandez, all of whom have emotionally supported me since starting this program.

I would like to extend my gratitude for everyone I have met in my time at the Smart Composites Laboratory; Dr. Junghun Wee, Dr. Jee Kim, Dr. Chia-Fu Wang, Anastasia Timofeeva, Sean Aiton, Sherif Hassan Aboubakr, Rohan Soman, Evan Youngberg, Md Raf E Ul Shougat, and Waliur Rahman. I couldn’t pick a better group of people to work with and learn around.

I would like to express my thanks to the Office of Naval Research (ONR) for funding my research endeavors.

TABLE OF CONTENTS

LIST OF TABLES vii
LIST OF FIGURES viii

Chapter 1: Introduction 1
1.1 Structural Health Monitoring Background 1
1.2 Ultrasonic sensing with FBG 3
1.3 Restoring Multiplexing Abilities in the Acoustic Domain 6
    1.3.1 Mode Propagation along optical fiber 6
    1.3.2 Potential of Acoustic Signal Multiplexing for Sensing Applications 9
    1.3.3 Previously Researched Acoustic Couplers 11
1.4 Scope of Research 13

Chapter 2: Performance and Stability Analysis of Cyanoacrylate Acoustic Coupler for Sensing Applications 16
2.1 Introduction 16
2.2 Methods 20
2.3 Experimental Results 25
    2.3.1 Signal Mapping 26
    2.3.2 Performance 33
    2.3.3 Repeatability 41
2.4 Discussion 47
2.5 Conclusion 48
2.6 Acknowledgements 49

Chapter 3: Laser Doppler Vibrometry Measurements of Acoustic Attenuation in Optical Fiber Waveguides 50
3.1 Introduction 50
3.2 Attenuation Measurement Methods 53
    3.2.1 Standard FBG Attenuation Measurement 53
    3.2.2 LDV Attenuation Measurement Methods 56
3.3 Attenuation Measurement Results 59
    3.3.1 Validation of LDV Attenuation Measurement 59
    3.3.2 Attenuation Coefficient of Silica Waveguides of Different Diameters 62
3.4 Conclusion 64
3.5 Acknowledgements 64

Chapter 4: Enhancing Cyanoacrylate Acoustic Coupler Performance through Flow Coating Fabrication 65
4.1 Introduction 65
4.2 Experimental Methods 69
    4.2.1 Coupler Fabrication 69
    4.2.2 Measurement of Coupler Performance 73
4.3 Results 75
    4.3.1 Performance of Flow Coated Coupler 75
    4.3.2 Decreasing Coupler Length Experiment 80

4.4 Conclusion 86
4.5 Acknowledgements 87

Chapter 5: Conclusions and recommendations for future work 88

REFERENCE 91

LIST OF TABLES

Table 2.1 Segment names and respective lengths 27

Table 2.2 Comparison of estimated and measured signal travel times 30

Table 2.3 Power measured at each FBG following first signal-coupler interaction 34

Table 2.4 Measured CA coupler signal transference performance 36

Table 2.5 Measured performance losses of the coupler 37

Table 3.1 Measured L_{01} attenuation coefficients for coated, single-mode optical fiber 61

Table 4.1 Measured power ratios for coupler ports. Molded coupler data from [54] 77

LIST OF FIGURES

Figure 1.1 Lamb wave velocity dispersion curves for aluminum plate (AL6061-T6, Thickness 2.1mm). (a) Phase velocity and (b) Group velocity [8] 2

Figure 1.2 Operating Principles of FBG [17] 4

Figure 1.3 (a) Optical component configuration for Edge filtering (b) Principle of edge filtering [26] [27] 6

Figure 1.4 (a) Direct bonding of FBG to measure Lamb waves (b) Remote bonding configuration of FBG [30] 7

Figure 1.5 Theoretical group velocity dispersion curves for the 135 μm polyimide coated optical fibre [33] 8

Figure 1.6 Example of distributed sensing network based on acoustic multiplexing 10

Figure 1.7 Composite CNT wrapping process for a SMOF 15

Figure 2.1 Potential distributed sensing network based on acoustic multiplexing 18

Figure 2.2 Experimental setup for measuring the performance of a 2-by-2 acoustic coupler 21

Figure 2.3 (a) Diagram of optical Fibers placed in Mold Core (b) Cross sectional view of the mold’s Cavity Plate (c) Picture of Mold in use 24

Figure 2.4 Stitched photograph of the acoustic coupler fabricated using 2.9 mm stainless steel mold 25

Figure 2.5 The coupled fiber network. Segment names in Table 2.1 and port names are labelled 27

Figure 2.6 (a) Incident signal prior to entering the coupler (b) The strain measured at each FBG following the initial signal-coupler interaction 28

Figure 2.7 (a) The layout of where each event occurred along each FBG path in the experiment; (b) legend for flow chart; and (c) Measured signals with flowchart added to describe signal packets path of travel through the network 32

Figure 2.8 Standard Deviation in Strain measurement between all 4 trials for each FBG 42

Figure 2.9 The standard deviation of relative waveform energy at each FBG following PZT excitation 45

Figure 3.1 Coupling of Lamb waves to optical fiber into the L_{01} mode in the remote bonded FBG configuration 51

Figure 3.2 Setup of the FBG based attenuation measurement 54

Figure 3.3 Setup of LDV based attenuation measurement 57

Figure 3.4 (a) Photograph of LDV setup and (b) schematic of silica rod with scan points indicated 57

Figure 3.5 Histograms that show distribution of the measured attenuation coefficients for (a) 44 measurements with the FBG method and (b) the 135 measurements taken with the LDV method........ 60

Figure 3.6 Attenuation coefficient of silica waveguides with and without polyimide coating 62

Figure 4.1 Potential distributed sensing network utilizing acoustic multiplexing 67

Figure 4.2 Schematic of the CA coupler flow-coating fabrication method........ 70

Figure 4.3 Composite Photo of: (a) 5.98 mm long coupler (coupler C) used in first experiment against checkered backdrop, (b) example of alignment-controlled coupler, and (c) 2.9 mm long molded coupler [54] 71

Figure 4.4 Aligned composite photo of: (a) flow coated acoustic coupler before length reduction, (b) after a single drop of acetone, (c) after a two drops of acetone, and (d) after a three drops of acetone 73

Figure 4.5 Experimental setup for measuring the performance of a 2-by-2 acoustic coupler 74

Figure 4.6 The relative power received by each port of the coupler as length was decreased for the (a) 1st long span coupler and (b) the 2nd short span coupler........ 81

Figure 4.7 The overall signal loss for the 1st long span and 2nd short span couplers........ 83

Figure 4.8 Plot of directional coupler performance across length showing; (a) the coupling factor and (b) isolation and coupling ratio of the 1st long span coupler, and (c) the coupling factor and (d) isolation and coupling ratio of the 2nd short span coupler 85

Figure 5.1 Quadrature Hybrid coupler with impedances of each line Y [47] 88

CHAPTER 1

Introduction

1.1 Structural Health Monitoring Background

Defects can be located and monitored over time by periodically measuring the dynamic response of a structure. The assumption is that the response exhibited will change as the defect forms. This process is known as structural health monitoring (SHM) and is often utilized to predict the remaining service life of a structure. There exists a variety of damage diagnostic techniques that can be used for SHM. However, ultrasonic based SHM is the most widely used due to its ability to perform robust localized assessments of a structure's health [1]. Defects can be detected sooner and located with a greater degree of precision by utilizing ultrasonic excitations. Since typically, the minimum defect size that can be detected with a SHM system is the same order of magnitude as the excitation wavelength [2], [3].

In SHM the pitch-catch method is a common example of how one would perform damage detection in the ultrasonic frequency range. In this technique an actuator is used to produce guided waves in the structure being analyzed. The guided waves propagate along the structure, distorting as they interact with any damage along their travel path. A sensor some distance away from the actuator will then measure the distorted wave. By then comparing this measurement to a reference waveform, information about the location and severity of damage can be identified [4], [5].

There are many types of guided waves, however, the most widely used for damage detection are Lamb waves. The utility of Lamb waves in SHM applications stems from their ability to propagate long distance while performing inspection through the thickness of the structure. Lamb waves are the result of an elastic perturbation on a thin structure with two free surfaces, such as a plate [1], [5]. Lamb waves form from the interference between guided longitudinal waves and polarized vertical shear waves [2], [6]. The different propagation modes of Lamb waves come in one of two forms, symmetric (S) and-anti symmetric (A). Identified by the type of deformation induced along the surface of the plate. The fundamental symmetric (S_0) mode corresponds to extensional deformation while the fundamental anti-symmetric (A_0) mode causes flexural displacements in the structure [7]. The number of modes excited in the plate as well as the velocity of each mode is dependent on plate thickness and the excitation frequency [2]. The dispersion curve for each of these modes in an aluminum plate can be seen in Figure 1.1. However, in this report only the S_0 and A_0 modes will be considered. These fundamental modes exist across the entire frequency spectrum and typically carry more energy than higher order modes, making them more useful for sensing applications.

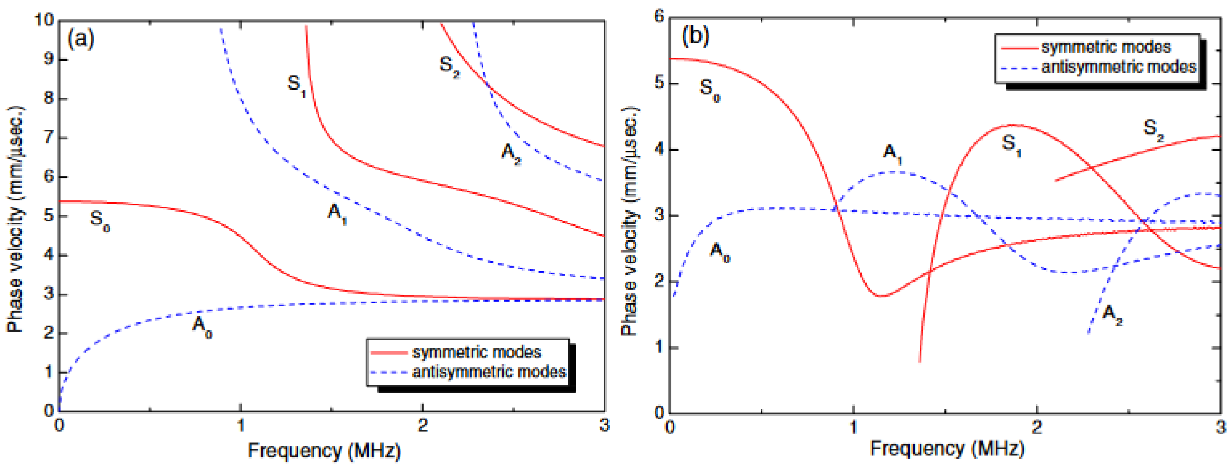

Figure 1.1 Lamb wave velocity dispersion curves for aluminum plate (AL6061-T6, Thickness 2.1mm). (a) Phase velocity and (b) Group velocity [8].

Fiber Bragg Gratings (FBGs) have become a popular choice as an acoustic sensor, they are lightweight, immune to electromagnetic interference, and they offer the ability to multiplex sensors easily. FBGs are already widely implemented in acoustic sensing of structures. Perez et al. [9]

demonstrated how FBGs could be attached to the surface of a structure for the purpose of measuring acoustic emissions.

Measuring ultrasonic Lamb waves with an FBGs has also been extensively studied [10], [11]. Betz et al. [12] provided one of the first FBG configurations capable of detecting an ultrasonic Lamb wave. Kirikera et al. [13] developed a passive impact monitoring system that used multiple FBGs to measure the Lamb waves excited from an impact. Which has since been more thoroughly explored by Frieden et al. [14]. Now mode propagation along optical fiber is being utilized to extend the sensing capabilities of FBGs. Tsuda and Lee [15] were one of the first to utilize mode propagation for sensing purposes, using a FBG to detect liquid on the surface of a structure. A similar type of detector was also made by Kim et al. [16] who used an acoustically coupled fiber ring resonator to monitor the rise in water levels. To enhance the range of capabilities in which mode propagation can be applied to FBG sensing, this paper will focus on minimizing losses along optical fibers and acoustic couplers.

1.2 Ultrasonic Sensing with FBGs

A FBG is an optical filter that is embedded in the core of an optical fiber. The grating lies within the core and consists of periodic changes to the refractive index along the length of the FBG. The period of the grating induces reflections across a narrow band of wavelengths allowing all other wavelengths to transmit through. FBG interaction with a broadband light source is demonstrated in Figure 1.2.

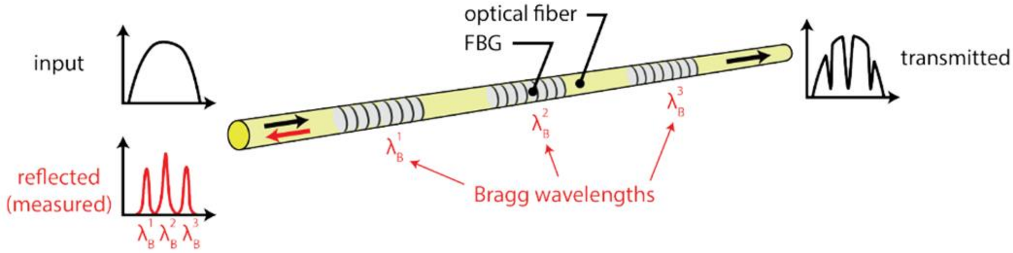

Figure 1.2 Operating Principles of FBG[17].

The maximum FBG reflectance occurs at the center of the reflected spectrum. Known as the Bragg wavelength, λ_B, its relationship to the effective refractive index, n_{eff}, and the grating period, Λ, is defined by,

$$\lambda_B = 2n_{eff}\Lambda \tag{1.1}$$

When compressive or tensile axial strains are imparted on the FBG, the grating period changes due to the elastic deformation of the fiber. So long as the wavelength of the ultrasonic signal is longer than the grating length, the entire reflected spectrum will shift without distorting in shape [18], [19]. This results in the entire reflected spectrum shifting linearly with FBG strain, demonstrated by Equation 1.2.

$$\frac{\Delta\lambda_B}{\lambda_B} = (1 - p_e)\varepsilon \tag{1.2}$$

where p_e is the photo-elastic constant for the silica optical fiber, and ε is the axial strain applied across the entire FBG grating. Thus, converting the mechanical deformation along the FBG into an optical signal. FBG have been proven to be effective acoustic sensors across a wide band of frequencies in the ultrasonic frequency range [11], [20], [21].

One of the most attractive features offered by FBG sensors is the ability to multiplex signals to the same fiber. With a broadband light source, the response of multiple FBGs can be monitored simultaneously through a process called wavelength division multiplexing [22], [23], [24]. However, this technique is limited to instances where low frequency (>5000 Hz) responses from the structure are expected. FBG interrogation devices are capable of directly tracking the Bragg wavelength of multiple FBGs, however, by performing spectral analysis the maximum acquisition rate of the device is severely limited. In addition, the overall shift in the reflected spectrum is relatively small. Therefore, directly tracking the Bragg wavelength lacks both the speed and sensitivity needed for ultrasonic sensing applications.

To circumvent these limitations, intensity based FBG interrogation methods such as the edge filtering technique are used. The setup for the edge filtering technique can be seen in Figure 1.3(a). This demodulation technique uses a narrow band tunable laser, to set the wavelength of the light source to half of max FBG reflectance. By monitoring the optical intensity reflected off the FBG at the fixed wavelength: a shift in the Bragg wavelength is observed as a change in the optical power [25]. Removal of the spectral component allows the use of high-speed photodetectors, increasing the overall measurement acquisition rate. The slope of the reflected spectrum scales the measurement response to strain, as seen in Figure 1.3(b) [17]. This allows the FBG to detect the small amplitude ultrasonic signals. However, without the spectral component the ability to multiplex FBG signals together is removed, limiting interrogation to one sensor at a time.

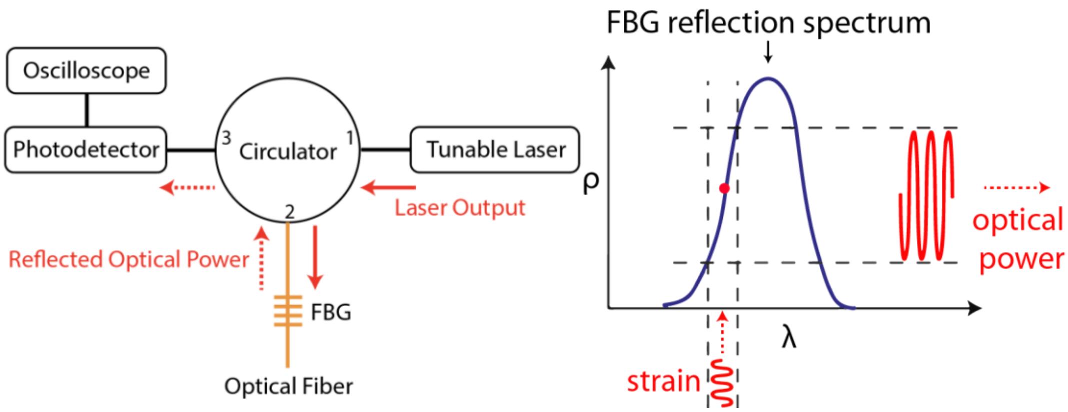

(a) (b)

Figure 1.3 (a) Optical component configuration for Edge filtering (b) Principle of edge filtering [26], [27].

1.3 Acoustic Multiplexing

1.3.1 Mode Propagation Along Fiber

Mode propagation along a single mode optical fiber (SMOF) has already been utilized as a means of directing acoustic signals [28], [29]. The silica fiber acts as a weakly guided waveguide that carries the acoustic signal to the FBG [15]. Wee et al. [26] demonstrated how this property of SMOF can be utilized in ultrasonic damage detection applications with the remote bonding technique. In the past FBGs were directly bonded to the surface of a structure to directly measure the Lamb waves. In the remote bonding configuration, the portion of the SMOF bonded to the plate is some distance away from the FBG. The Lamb waves are confined to the SMOF as an extensional signal before the signal is guided to the FBG. The direct bonding and remote bonding configurations can be seen in Figure 1.4(a) and Figure 1.4(b) respectively.

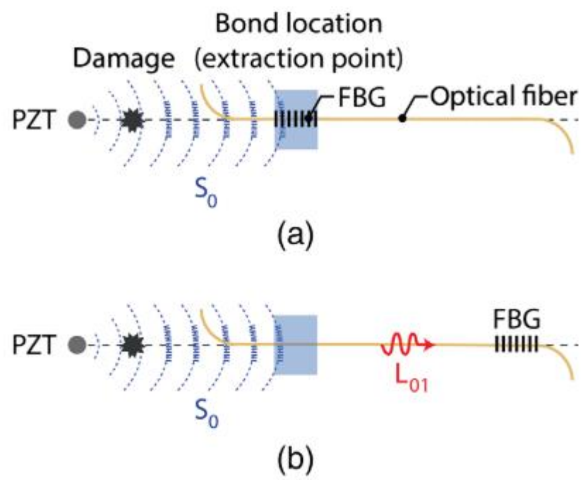

Figure 1.4 (a) Direct bonding of FBG to measure Lamb waves (b) Remote bonding configuration of FBG [30].

In remote bonding the S_0 and A_0 mode Lamb waves in the plate are converted to the longitudinal L_{01} and flexural F_{11} modes along the optical fiber. The flexural mode attenuates quickly and will not cause deformations that affect the period of the Bragg grating. So, the presence of the flexural mode can be effectively ignored. The longitudinal mode will travel along the optical fiber with minimal attenuation [31]. The FBG will then measure the L_{01} mode as it passes, since the mode shape causes mechanical deformation along the pitch of the grating[19], [32]. For a typical SMOF, the L_{01} mode is nondispersive up to 10 to 15 MHz [33]. The dispersion curve for polyimide coated SMOF can be seen in Figure 1.5. For these reasons the longitudinal mode is an excellent signal to use for FBG based ultrasonic sensing. Furthermore, with no adhesive to limit the strain induced along the FBG, the remote bonding technique also results in higher amplitude measurements.

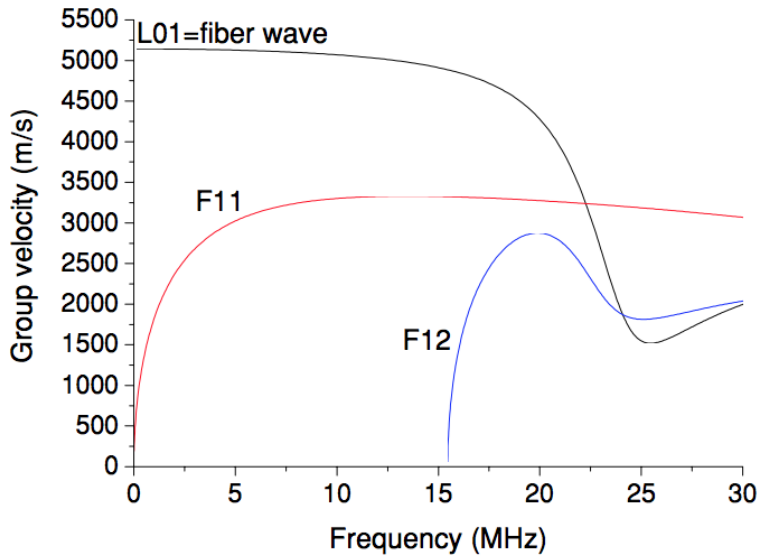

Figure 1.5 Theoretical group velocity dispersion curves for the 135 μm polyimide coated optical fibre [33].

For this work it is important to also point out the differences between acoustic and optical mode propagation along the SMOF. For the optical mode, both the core and cladding of a typical SMOF are made of silica with a final polymer coating added for durability. In this case the optical mode is completely confined to the core due to the optical index of refraction distribution across the fiber cross-section. In contrast when a SMOF is used as an acoustic waveguide the L_{01} mode will not be confined to any region of the cross section. When the wavelength is much larger than the overall diameter of the waveguide the wave will not interact with the cladding and core layers independently. The wave will propagate as if it were traveling along a homogenous rod possessing acoustic properties that are some aggregate of the polymer and silica materials [34]. A typical sensing frequency of 300 kHz will result in a wavelength of 17 mm along a SMOF, far exceeding the diameter of the optical fiber. Demonstrating that regardless of the frequency used the wavelength of the signal will greatly exceed the overall diameter.

Another key difference in how the L_{01} mode propagates along the SMOF is leakage. The longitudinal modes are not strictly guided but are instead prone to mode leakage through the waveguide's radius [35]. Mode leakage introduces an additional factor that contributes to acoustic signal loss along the SMOF. The attenuation due to power leakage is dictated by the difference in the shear-velocity and density between the core and cladding layers [36]. Ideal mode guiding behavior will only occur when the shear-velocity and density of both layers are equal.

In short, any additional mass added to the surface of the SMOF will affect L_{01} mode propagation along the SMOF. The small diameter relative to wavelength predicts the added mass will result in a change in the acoustic properties of the region. Resulting in impedance mismatches that will cause partial reflections of the L_{01} mode. In addition, the leaky nature of the longitudinal mode suggests that the acoustic signal power will leak into any component added to the SMOF surface. The differences between optical and acoustic mode propagation along a SMOF illustrate the difficulty of fabricating components that interact with the acoustic signal without incurring more signal losses.

1.3.2 Potential of Acoustic Signal Multiplexing for Sensing Applications

The current major limitation of FBG use within ultrasonic SHM systems stems from the inability to multiplex individual optical signals when using the edge filtering configuration. Restoring the ability to multiplex signals from the structure would reduce reliance on optical components and would extend the range of applications where FBGs can be utilized for ultrasonic SHM.

One potential workaround is to perform multiplexing in the acoustic domain before the signal is measured by the FBG. This setup would consist of two types of waveguides, the transmission fibers and the remote sensing fiber, seen in Figure 1.6. The transmission fibers are responsible for transferring the Lamb waves from the plate to the remote sensing fiber by guiding the L_{01} mode. These fibers primarily act as acoustic waveguides, so they can be made of any material since they are not optically connected to the rest of the system. The signal from each transmission fiber is combined along the remote sensing fiber, which houses an FBG that is used for measuring the multiplexed acoustic signals. Thus, producing a distributed sensing network that can monitor multiple locations in a structure while utilizing only one FBG.

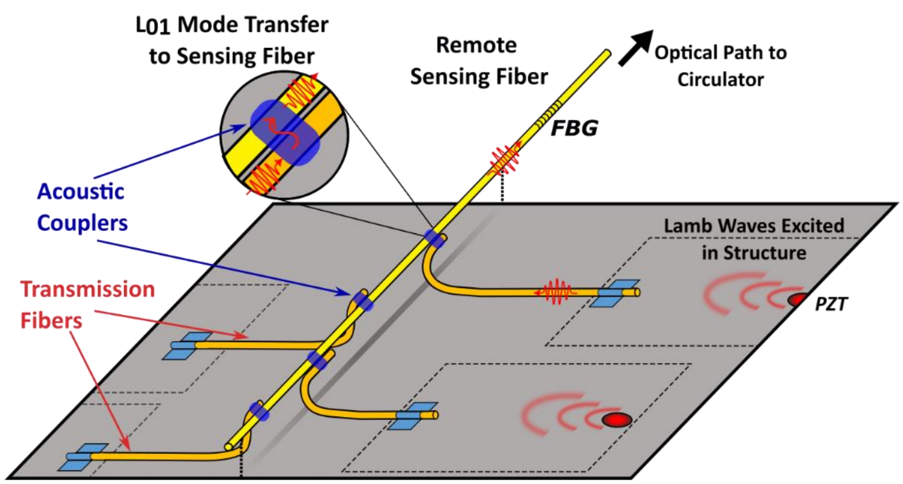

Figure 1.6 Example of distributed sensing network based on acoustic multiplexing.

To achieve this, a reliable method of transferring acoustic information from one waveguide to another must be developed. In other energy domains signal transfer between waveguides is performed with passive directional signal couplers. An acoustic variant of such device was theoretically described by Safaai-Jazi, who modeled the coupling coefficient between two parallel acoustic waveguides that share a common cladding [37]. This work is predicated on coupled mode theory which is used to describe the behavior of fused optical fiber couplers. Coupled mode theory predicts a periodic relationship between the coupler's length and the power distribution across the two fibers. This behavior was also predicted by an energy-based spring-damper model by Schaal et al. [38] who used the model to simulate the signal coupling between aluminum wires.

Recently Kim et al. [39] fabricated a CA acoustic coupler to experimentally demonstrate multiplexing of acoustic signal. Utilizing a similar configuration seen in Figure 1.6, they reported being able to monitor three damage locations in a plate using a single FBG sensor. While acoustic signal multiplexing was successfully performed, the number of waveguides that can be coupled to a single sensor was limited as losses increased with each additional waveguide. Furthermore, the effectiveness of this technique is severely limited by input reflections and losses through the coupled region of the network. Since the ultrasonic pitch-catch method relies on the sensor detecting the difference between two waveforms, the technique requires the FBGs receive large amplitude signals from the structure [3]. Therefore, if acoustic signal multiplexing is to be implemented in SHM, minimizing any source of loss along the path to the FBG is critical.

1.3.3 Previous Research into Acoustic Coupling

Only recently has there been research into fabricating an acoustic coupler suited for acoustic signal transference in SHM. Prior to this there were few attempts to manufacture acoustic couplers for optical fibers. Most notably, Matthews et al. [40] conducted a study on the acoustic coupling observed in a fused core coupler they produced. The opto-acoustic coupler in this experiment was fabricated by twisting the strands of the glass fiber together applying heat then pulling glass fibers until they fused. They reported that excess losses and coupling efficiency was best with a long gradual taper to coupler shape. The coupler tested was successful in transferring the acoustic mode from one fiber to another, however, they listed asymmetrical power splitting, high insertion losses, and excesses losses as major performance limitations.

Theory suggests that a fused core coupler would exhibit optimal performance and more homogenous properties, since no additional mass is incorporated during fabrication. However, the fabrication technique is impractical for SHM applications. Using heat to fuse the silica results in brittle connections and is difficult to perform in the field and impossible to undo. Coming up with a robust acoustic coupler that can be easily applied in the field is key for creating an effective tool for SHM purposes. For this reason, many previously studied couplers are made of Cyanoacrylate (CA) adhesive applied to the surface of the two waveguides.

Kim et al. [41] was one of the first to demonstrate the signal transference capabilities of CA coupler. In this experiment acoustic signal was transferred between waveguides with miss matched geometries. Kim et al. was not able to control the adhesive coupler length to control the coupling ratio between the two fibers. In optical couplers, the coupling efficiency is governed by the ratio of the coupler length and the mode wavelength in the fibers. So, to minimize losses due to the adhesive, they decided the amount of CA used in fabrication was to be kept to the absolute minimum. They found that a drop of adhesive was sufficient to create coupling. This technique was again used to produce a fiber ring resonator and demonstrate acoustic signal multiplexing [16], [39]. However, in each of these applications the insertion losses and input reflections heavily limited signal transfer to the opposite fiber.

This dissertation will focus on modifications to the couplers themselves that improve signal transference. However, producing an adhesive coupler whose cross section is uniform across its length is a challenge that must be addressed. Uniformity ensures the acoustic properties of the coupler are uniform with no abrupt changes [36]. In addition, the amount of CA used during fabrication must be balanced as using less CA will result in a much more fragile bond.

1.4 Scope of Research

The objective of this work is to explore practical methods for preserving and transferring the L_{01} mode along coupled waveguides. Our focus will be aimed towards acoustic waveguide networks that can be used for FBG based sensing applications. So, silica SMOFs were used as the primary acoustic waveguides in these experiments. To complete this objective two main avenues were considered: first, exploring coupler design to enhance signal transference to the FBG and second, minimizing the acoustic attenuation through any portion of the waveguide network. A detailed list of the research objectives are as follows:

1. Experimentally investigate acoustic couplers and determine what characteristics influence the coupler's performance as a directional coupler.
2. Develop and experimentally verify a novel method for measuring acoustic attenuation in non-single mode optical waveguides.
3. Evaluate the effect diameter has on acoustic signal attenuation across the length of silica waveguides.
4. Investigate potential surface treatments for reducing signal attenuation along the fiber.
5. Further refine the fabrication process for acoustic couplers to minimize the input reflections and signal loss.

Chapter 2 investigates the performance of the CA coupler fabricated with a stainless-steel mold. In this experiment mode propagation through a 2-by-2 coupler will be monitored with 4 FBG along each port. The same criteria used for passive directional couplers will be applied to characterize performance of the coupler for comparison. Results reveal the L_{01} mode propagated along the entire coupled fiber network consistently. Shortcomings with the coupler design will be identified by comparing the results with conventional couplers. Which will reveal how the longitudinal mode interacts with the CA coupler.

Chapter 3 introduces a novel LDV based method for measuring the acoustic attenuation across non-optical waveguides. The technique will then be compared to an established FBG based method to verify the validity. Once established, the method will be used to measure the acoustic attenuation along silica rods and fibers of various diameters. This experiment will demonstrate that as the diameter of the silica rod decreases the signal loss per waveguide length increases. Which shows that mode leakage is the primary source of signal loss along a thin SMOF.

Regarding completing research objective 4, a composite carbon nanotube (CNT) wrap was developed to reduce signal attenuation along a SMOF. Figure 1.7 shows the setup used to apply the composite wrap on the surface of the SMOF. A motorized take-up spool slowly pulled the fiber through the wrap head. Spinnable CNT was applied along the surface of the fiber as the wrap head spun. Finally, an adhesive-acetone solution is applied to consolidate the final wrap. Both TPU and Epoxy 400 were used in the consolidation solution. The signal attenuation across the wrapped portion of the fiber is measured with two FBG. However, the results of this experiment indicate that signal loss along the optical fiber increases with the application of the composite wrap. Therefore, this work will not be included in the dissertation.

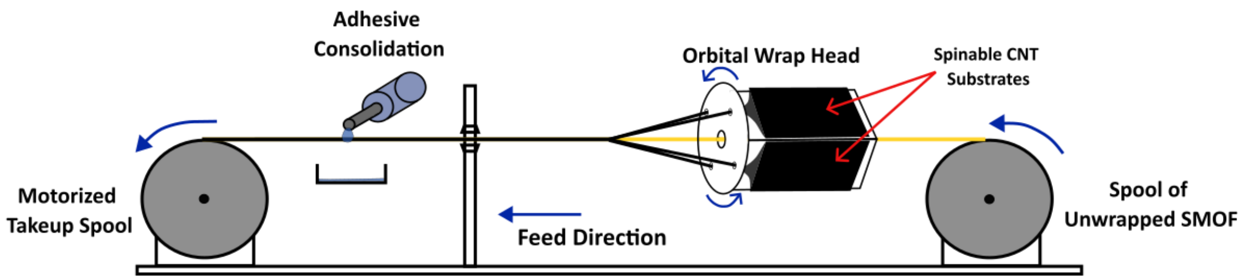

Figure 1.7 Composite CNT wrapping process for a SMOF.

Chapter 4 explores a flow coating-based method for fabricating CA couplers. This design is intended to address the design limitations discussed in Chapter 2. By dissolving the CA adhesive in acetone before applying the solution to two closely spaced SMOF. Capillary forces between the fibers will limit the adhesive deposited. Couplers fabricated with this method will be compared with those fabricated with the mold in Chapter 2. Demonstrating that signal losses were dramatically reduced by limiting the CA deposited. This experiment will also observe the performance of CA couplers as the length of the coupler decreases. These results reveal that the length had no major effect on performance outside of those associated with material losses.

Finally, Chapter 5 reviews the results summarizing findings and presents recommendations on further refining the acoustic coupler design in the future.

CHAPTER 2

Performance and Stability Analysis of Cyanoacrylate Acoustic Coupler for Sensing Applications

In this paper the performance of cyanoacrylate (CA) acoustic signal coupling device with known geometry will be explored. A stainless-steel mold was used to create a 2-by-2 CA coupler that transferred guided waves between two optical fibers. Four FBGs placed at each port were used to assess the repeatability, general behavior, and performance of the coupler produced. Signal propagation through the network was mapped to determine how the initial acoustic signal traveled and subdivided through the fiber network. To look at the stability and repeatability of the signal coupler interaction when all factors were held constant the experiment was completed an additional 3 times. Finally, the acoustic energy transferred through the coupler's paths were calculated to assess the performance of the 2-by-2 coupler. The coupler fabricated for this experiment successfully and repeatably transferred an acoustic signal from one optical fiber to another, however, the performance associated with the current coupler design was limited by relatively large excess and return losses. Improvements to CA coupler design were then identified from the results so that an acoustic coupler, capable of robust signal transference, can be developed in the future.

2.1 Introduction

Fiber Bragg Gratings (FBGs) have become a popular choice for the detection of ultrasonic Lamb waves within the field of structural health monitoring (SHM) [1], [13], [31], [42]. When ultrasonic waves pass along an FBG the induced axial strain along the optical fiber changes the properties of the FBG and shifts the reflected spectrum in the wavelength domain

[17], [18], [22], [42]. The time-dependent shift in the spectrum is linearly related to the waveform of the ultrasonic guided wave. Unlike for strain or vibration monitoring applications, measuring the shift in the Bragg wavelength directly does not provide sufficient resolution to detect the low amplitude guided waves [43]. Edge filtering is the most common method used to increase the FBG sensitivity and acquisition rate sufficient for guided wave detection [25], [44], [45]. A narrow bandwidth source (e.g. a tunable laser) is tuned to the midpoint of the linear portion of the FBG's reflected spectrum. Therefore, the wavelength shift in the FBG reflected spectrum is converted into a change in the output reflected power which is measured by a photodetector. The sampling frequency is only limited by the photodetector and oscilloscope [17], [25]. Unfortunately, while the edge filtering technique can reliably measure the response of a FBG to guided waves, it removes the ability to multiplex multiple FBGs in a single channel and limits the number of sensors to one FBG per filter and photodetector combination. In contrast, FBG instrumentation that utilizes wavelength or time division multiplexing does not possess the sampling frequency or sensitivity required to reliably measure Lamb wave amplitudes in the ultrasound frequency range [23], [24] .

Recent research demonstrated that the sensitivity of FBGs to guided waves (in this case Lamb waves) can be enhanced through a technique referred to as remote bonding [26]. In the remote bonding configuration, the portion of the optical fiber bonded to the plate is some distance away from the FBG. Symmetric (S) and antisymmetric (A) Lamb waves are both converted into extensional L_{01} and flexural F_{11} modes at the adhesive bond, which propagate along the optical fiber. The L_{01} mode travels along the optical fiber before reaching the FBG while the flexural mode attenuates quickly. Thus, the silica fiber acts as a weakly guided acoustic waveguide that carries the ultrasound signal to the FBG [36]. The L_{01} mode along a single-mode optical fiber is nondispersive at ultrasonic frequencies below a few MHz and possesses a mode shape that causes axial deformation along the FBG grating [19], [32], [46]. In addition, as the FBG is not constrained by the adhesive, the L_{01} mode creates a larger spectrum shift, resulting in higher amplitude measurements. However, remote bonding does not solve the lack of multiplexing capabilities for edge filtering, which is a barrier to developing a comprehensive real time damage diagnostic system for a large structure.

One solution to multiplexing is to use acoustic couplers to couple the ultrasonic waveform from multiple optical fiber waveguides to a single fiber waveguide, similar to the concept of an optical fiber coupler. In the potential acoustic coupler-based fiber sensor network multiple acoustic transmission lines would be bonded to points of interest along the structure, as shown in Figure 2.1. The ultrasound signals carrying structural information are guided from each point of interest then transferred from the transmission line to a SMOF that houses a common FBG that will be used for the measurement.

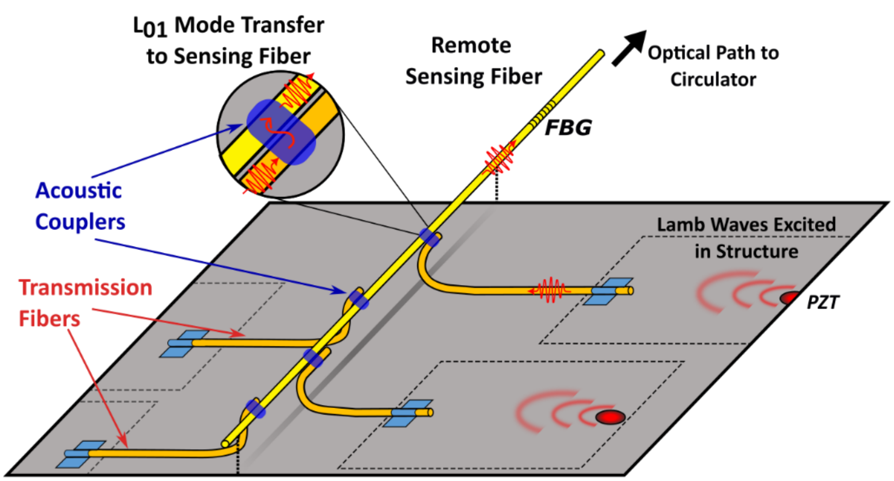

Figure 2.1 Potential distributed sensing network based on acoustic multiplexing.

Early investigations into acoustic couplers studied the transmission of ultrasonic waves through fused optical fiber couplers. For example, Matthews et al. [40] fabricated an acousto-optical coupler by heating the silica fibers and twisting the strands together until they fused. The coupler tested was successful in coupling the acoustic mode from one fiber to another, however the performance was severely limited due to high insertion losses. Additionally, the coupler fabrication process is complex and cannot be rapidly applied in field applications. For these reasons, Kim et al. [41] demonstrated an adhesively bonded optical fiber acoustic coupler. While the mode propagation of the light is entirely confined near the core of the optical fiber, the ultrasonic mode is distributed throughout the optical fiber cross-section due to its much larger wavelength. As long as the coating is thin, the mode propagates as a weakly guided mode, continuous at the cladding-core interface [34] Therefore, tapering and fusing of the two optical fibers to create overlap of the two core regions is not necessary and ultrasonic waves were transmitted through the adhesive bond.

Kim et al. [41]experimentally demonstrated that a cyanoacrylate (CA) bond coupled ultrasonic waveforms between fiber waveguides, fiber waveguides with mismatched geometries, and fiber waveguides with different materials. Kim et al. [16] also experimentally demonstrated that the original waveform was preserved after transfer through the adhesive coupler. However, similar to the fused silica coupler results, the losses in the signal were high [16]. The authors did not investigate whether these losses were due to reflections of waveforms from the adhesive bond, partial absorption of the wave by the CA polymer, or poor signal coupling resulting in the majority of signal energy remaining along the original fiber.

The acoustic coupler's performance as a directional coupler and as a component along a signal transmission network has yet to be thoroughly investigated. This paper aims to further develop real world adhesive-based couplers with an in-depth performance analysis of the CA coupler presented by Kim et al [41]. By measuring the strain along each FBG after PZT excitation we can decern how the signal moved through the coupled fiber network.

The measured path lengths of the fiber network are used with the known wave speed along the SMOF at 300 kHz to estimate the potential time difference between any two FBG measurements. With these values a map of the acoustic signal's path of travel through the fiber network can be determined from the strain data. Next, the strain packets are quantified in terms of power relative to the initial signal (pre-coupler interaction) so the performance as a directional coupling device can then be gauged. With this, the performance of the CA coupler will be presented using the same specifications used for other coupling devices. This analysis will then be used as a basis for determining the source of limitations associated with the current acoustic coupler design. Finally, by performing this experiment across multiple trials the stability of the signal's interaction with the entire fiber network can be monitored. Calculating the deviation between each trial will monitor how variations in signal energy propagate through the CA coupled fiber network. Determining the suitability of the CA coupler for FBG based sensing applications.

2.2 Methods

The experiments in this paper were performed to monitor acoustic signals as they propagate through a 2-by-2 adhesively bonded optical fiber coupler (as shown in Figure 2.1) and to measure coupling performance of the coupler through each branch. Figure 2.1 depicts an example path the acoustic signal would travel in a coupled fiber network that would be used for SHM. This configuration was used for the experiments. The PZT generates symmetric (S_0) and antisymmetric (A_0) Lamb waves which travel along the structure (aluminum plate) before reaching a CA thin film that bonds the SMOF to the surface of the plate. The Lamb waves in the structure are measured at this location. The film converts the Lamb waves from the structure to the SMOF as a longitudinal (L_{01}) mode, preserving the waveform of the original signal. The L_{01} mode is then guided along the SMOF waveguide where it enters one of the ports of the 2-by-2 coupler. At the coupler, the signal is then split between the two fibers and is detected by FBG sensors (FBG 1 and FBG 3) in each fiber. These fibers will be referred to as the unbonded and plate bonded SMOFs. For the purposes of this paper, additional FBG sensors were added to capture the input signal (FBG 2) and the signal propagated in the reverse direction in the unbonded SMOF (FBG 4) and the plate bonded SMOF (FBG 2), however these are not needed for most SHM applications.

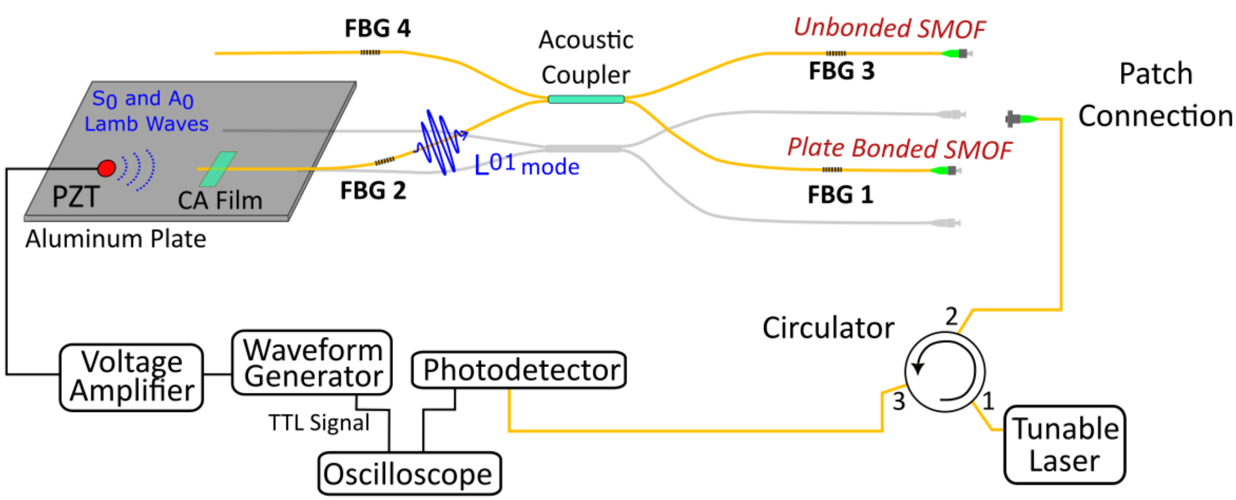

Figure 2.2 Experimental setup for measuring the performance of a 2-by-2 acoustic coupler.

A PZT and an aluminum plate were used to create a clean extensional signal to use as the input into the coupler. The PZT produces S_0 and A_0 Lamb waves in the 609.6 mm x 609.6 mm and 0.8 mm thick 6061 aluminum plate. The edges of the plate were covered with 7.62 cm wide strips of an elastomeric damping material (Dynamat®) on both sides to damp signals and prevent signal reflection at the plate edges. The PZT was placed at the center of the plate, 22.86 cm from the edges of the Dynamat strips. The end of the plate bonded SMOF was embedded within a rectangular 2 cm by 1 cm CA film on the aluminum plate, at 10 cm away from PZT so the S_0 and A_0 modes had fully separated. Both fibers used in this experiment were standard single mode optical fiber (SMF-28e) with a 15 µm thick polyimide coating. The PZT was actuated by an arbitrary waveform generator (AWG) and amplifier that produced 5.5 cycles of a 300 kHz Hanning windowed function every 10 milliseconds [21]. The trigger signal from the AWG was used to synchronize the oscilloscope measurement window with the excitation period.

The L_{01} signal that arrived at each FBG was measured with the edge filtering technique. The fiber connections to the circulator were manually switched. After connection, the reflectance spectrum of each FBG in the fiber was measured to calibrate the edge slope and the tunable laser was tuned to the midpoint of the rising edge of the first FBG. The deformation of the FBG due to the L_{01} signal was converted to a voltage at the photodetector (PD) and recorded with the oscilloscope. The signal acquisition of the oscilloscope was time synchronized with the PZT excitation signal from the AWG using a TTL trigger signal. The sample rate was 5 GHz across the 10 ms window. The strain measured by each FBG across the measurement window was averaged 4,096 times using the oscilloscope to remove noise, critical since the mode amplitudes are low. This measurement was then repeated 3 more times for the repeatability analysis. Afterwards, the process was repeated for the second FBG in the fiber, and then the other fiber connected, and the process repeated for the other two FBGs.

The coupler was fabricated through adhesive bonding, following the technique of Kim et al. [41]. The goal is to create a coupler that can be rapidly fabricated in field SHM applications. Cyanoacrylate (CA) was chosen as the adhesive since previous experiments have shown that it is capable of transferring Lamb waves from a plate to an optical fiber as well as from waveguide to another [16], [26], [41]. While higher molecular weight polymers have more favorable acoustic properties, they are significantly harder to work with and often require a catalyst for polymerization. The goal of this paper is not to optimize the coupler, but instead to understand the wave coupling behavior through the coupler.

The CA was applied to the two optical fibers using a stainless-steel mold which can be seen in Figure 2.3. The mold was designed to fabricate CA couplers that were 3.175 mm in length and consisted of two parts: the core, and the cavity plate. These pieces fit together to form the cavity which forms the final shape of the coupler. A channel was laser cut channel down the center with a radius of 0.381 mm, which acted as an alignment guide for the two fibers. While the cavity plate was designed to help ensure the CA was evenly distributed with the excess adhesive forming a flash away from the coupler so that it could be trimmed. Assuming ideal release from the mold, the final acoustic coupler would have a semi-circular cross section the same radius as the laser cut channel. Prior to applying the CA adhesive to the mold, a generous layer of LPS dry silicone lubricant was applied to the mold surface followed by a thin layer of water based polyvinyl alcohol (PVA) to prevent coupler adhesion to the mold. The CA coupler was given 12 hours to cure before it was removed from the mold. Excess CA was trimmed off before the sample was tested.

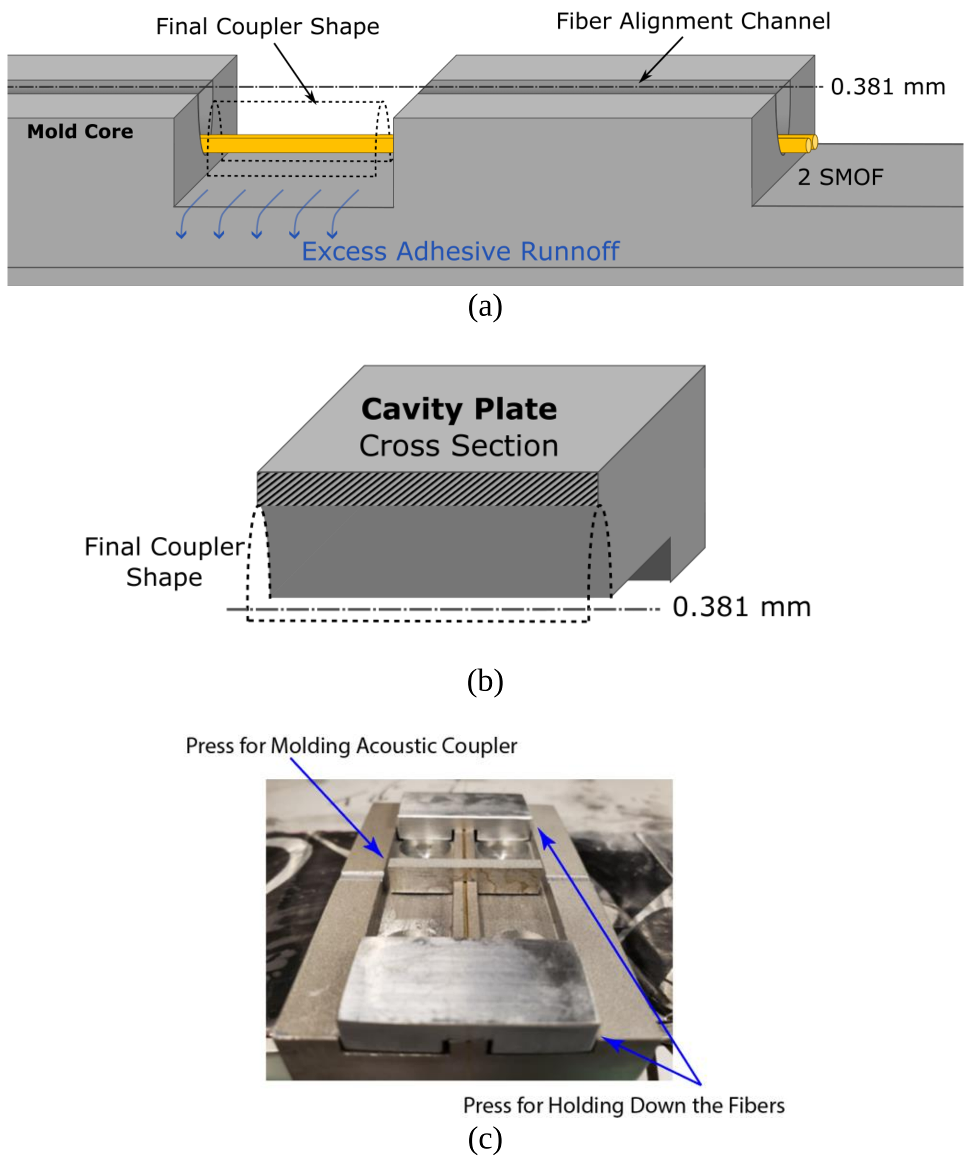

Figure 2.3 (a) Diagram of optical Fibers placed in Mold Core (b) Cross sectional view of the mold's Cavity Plate (c) Picture of Mold in use [41].

While the mold was specifically designed to produce a coupler with a uniform semi-circular, cross section images taken of the coupler showed this was not the case due to difficulties in removing the flexible polymer from the mold. The fibers were in contact for the full length of the coupler, however the cross section of the outer diameter of CA was irregular across the coupler length, as can be seen in Figure 2.4 which shows a composite image of the coupler used in this experiment. Based on previous experiments [41], the excess CA adhesive can create more loss in the coupler but does not prevent coupling between the two fibers. Future work is needed to improve the coupler fabrication process for repeatability between different couplers. The dimensions of the coupler were measured with calipers. The CA acoustic coupler used in these experiments was 2.9 mm long and had a maximum width of 0.45 mm. To assess the repeatability of the coupler performance, the same coupler was used in all four trials with all other factors held constant.

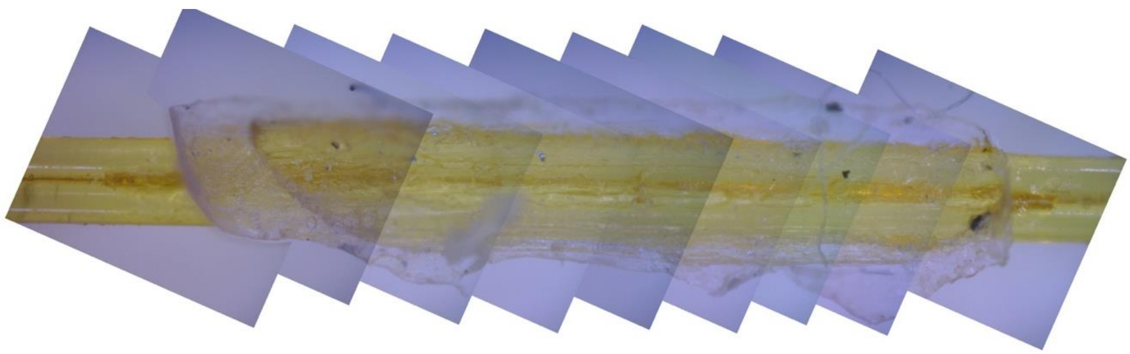

Figure 2.4 Stitched photograph of the acoustic coupler fabricated using 2.9 mm stainless steel mold.

2.3 Experimental Results

Measurements of the ultrasonic wave propagation through each fiber in the acoustic coupler were performed for the 2.9 mm long coupler. The data was used to map how the signal traveled through the coupled fiber network, including multiple interactions with the coupler and the reflections off the optical fiber ends. The arrival time of the ultrasonic wave packets were compared with the predicted signal arrival times to decern the direction and path the signals traveled within the 2-by-2 fiber network. Next, the acoustic energy sent to each port of the coupler was calculated so that the performance of the acoustic coupler could be assessed. Finally, the repeatability of the signal coupling was analyzed by repeating the experiment three times and calculating the variance between all four trials of the experiment. Between each trial of the experiment, the FBG sensors were recalibrated.

2.3.1 Signal Mapping

Figure 2.5 shows the position of each FBG in the experiment and the designated name for each port of the 2-by-2 coupler. As well as labels for the different segments used in the time of arrival calculations and the port names for the coupler. The signal excited by the PZT was coupled to the plate bonded fiber at the CA film and passed FBG 2 prior to reaching the coupler. At the coupler the signal was then subdivided along all four branches of the network. The subdivided signals travelled along their respective fiber and reflected off the end of the fiber. If strong enough, the signal would propagate back to the coupler and repeat subdivision. The first goal of the experiment was to map out which wave packets corresponded to which signal pathways. The multiple branches complicated signal mapping, therefore, the length of the different segments was chosen to make each path length unique. The signal paths were divided into segments, shown in Figure 2.5, based on each FBG location. The length of each fiber path segment was measured (± 1 mm) and is listed in Table 2.1.

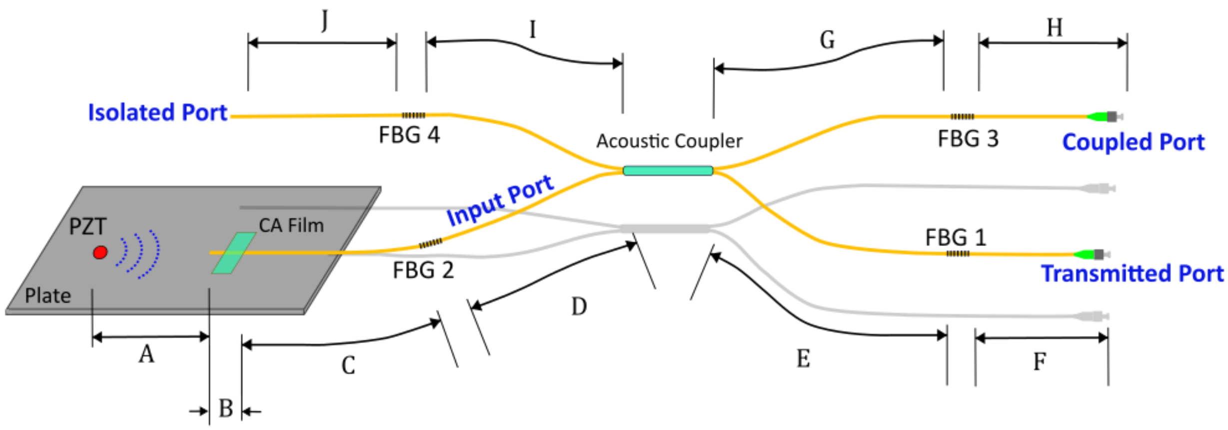

Figure 2.5 The coupled fiber network. Segment names in Table 2.1 and port names are labelled.

Table 2.1 Segment names and respective lengths.

Segment Name	Length (mm)
A	100
B	10
C	353
D	301
E	241
F	140
G	257
H	101
I	241
J	215

Only a single waveform was transferred from the plate to the fiber. This signal was measured by FBG 2 prior to reaching the coupler. The initial waveform, plotted in Figure 2.6(a), arrived 110 µs after PZT excitation and took 70.0 µs to completely pass FBG 2. The initial signal continued to propagate to the coupler. The strain measured by each FBG following the first interaction with the coupler is plotted in Figure 2.6(b).

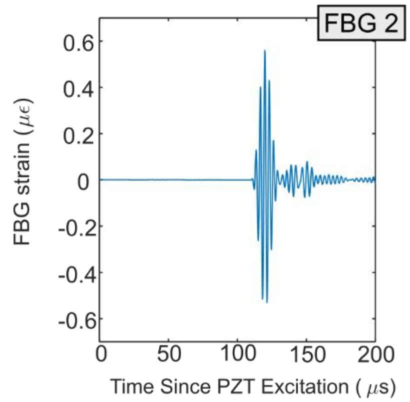

(a)

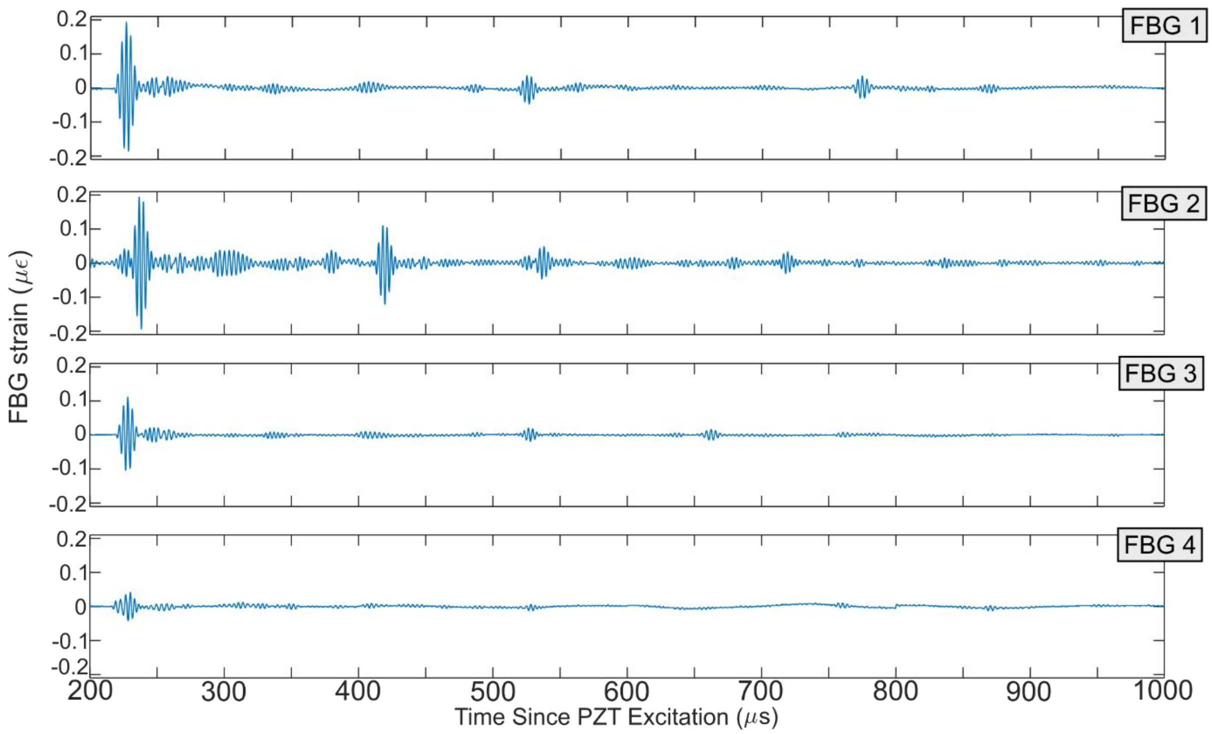

(b)

Figure 2.6 (a) Incident signal prior to entering the coupler (b) The strain measured at each FBG following the initial signal-coupler interaction.

Using the dimensions of the segments listed in Table 2.1 and known wave speeds, the expected delay between each FBG measurement was predicted, including reflections from the fiber ends and the CA film. The pathway to each signal in Figure 2.6 was then determined by comparing the theoretical signal arrival times to the measured results. The wave velocity of the ultrasonic L_{01} mode along the polyimide coated SMF-28e optical fiber and the S_0 mode through the 0.8 mm thick aluminum plate at 300 kHz are 5,110 m/s and 5,390 m/s respectively [26]. The wave velocity through segment B, the region with the CA film on the plate was not known, and so was estimated from the arrival time of the first signal at FBG 2 from Figure 2.6(a). The estimated velocity was 464.7 m/s, much slower than the L_{01} or S_0 mode, as expected. Wee et al. [30] used a similar fiber bonded to an aluminum plate with a strip of adhesive tape and found that the wave velocity in the taped region was 250 m/s. As the adhesive tape has a much lower modulus than the CA film, this gives confidence that the estimated velocity from these experiments in segment B is correct.

After the first coupler interaction the acoustic signal was now subdivided along the 4 paths of the fiber network. The reflected portion of the first signal-coupler interaction (along the FBG 2 path) traveled back to the fiber-plate bond where it reflected off the CA film and eventually reentered the coupler. The second signal-coupler interaction occurred after the signal passed FBG 2 roughly 410 μs after PZT excitation, where signals were again measured by each FBG 105 μs later. The secondary signal coupler interaction was identified by the spacing of the signals as they aligned with the first interaction. While the effect of the CA lowering the overall wave speed has been established, the delay that resulted from the 2.9 mm coupler was too small to observe in the results.

Using the arrival time of the waveform as the point of reference, the actual time difference between each signal packet was calculated and compared to the measured values. The predicted Δt between two measurements as well as the measured Δt is shown in Table 2.2, which shows the main paths that signal would have taken within the coupled fiber network. The measured time of arrivals between each FBG measurement matched closely to one of the predicted time of arrivals. Using Table 2.2, the path of travel for each signal in Figure 2.6 was determined and used to create the flowchart of signal pathways in Figure 2.7. This allowed all wave packets that were recorded to be linked back to the original waveform that entered the coupler from FBG 2.

Table 2.2 Comparison of estimated and measured signal travel times.

Path	Path Composition by Segment	Total Path Length (cm)	Measured Δt (μs)	Predicted Δt (μs)	Percent Difference (%)
PZT → FBG 2	A + B + C	42.3	109.4	109.15	0.22
FBG 2 → FBG 2	2D	60.2	120.4	117.81	2.15
FBG 2 → FBG 2	2(B+C)	72.6	181.2	181.69	0.27
FBG 2 → FBG 1	D + E	54.15	107.2	105.97	1.15
FBG 1 → FBG 1	2F	279.1	545.6	546.18	0.1070
FBG 2 → FBG 3	D + G	55.65	109.6	108.90	0.6350
FBG 2 → FBG 4	D + I	54.2	106.2	106.07	0.1257
FBG 4 → FBG 4	2 J	43	82	84.15	2.62

The results of this analysis show the ultrasonic L_{01} signal did pass multiple times through the acoustic coupler, as expected. However the amplitude of the signal did decay significantly with each pass, so many reflections do not need to be considered. Additionally, there was no interference between the propagating signals. Choosing different lengths for each FBG path along the fiber network helped differentiate signal movement within the network and ultimately determine the source of each signal packet measured in the experiment. However, for applications where the branches have similar lengths overlapping signal packets may occur.

Next, we will calculate the actual coupling parameters based on the wave packet energies.

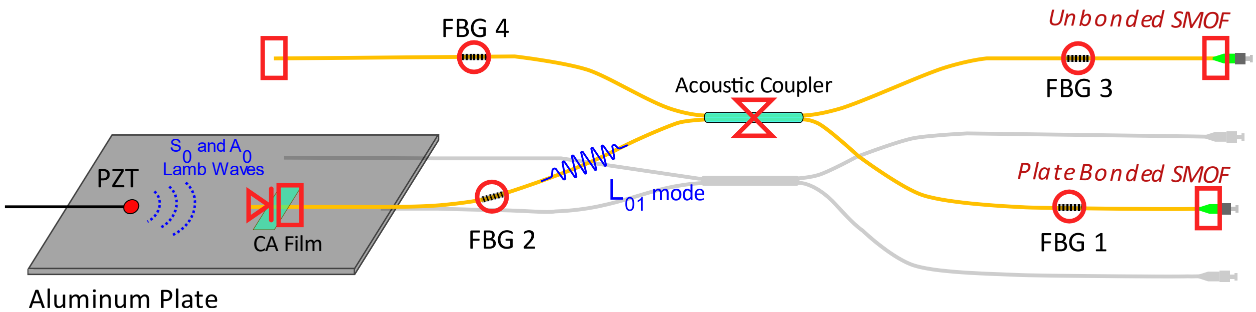

(a)

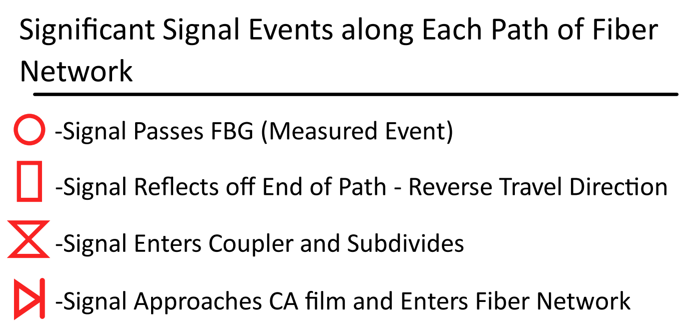

(b)

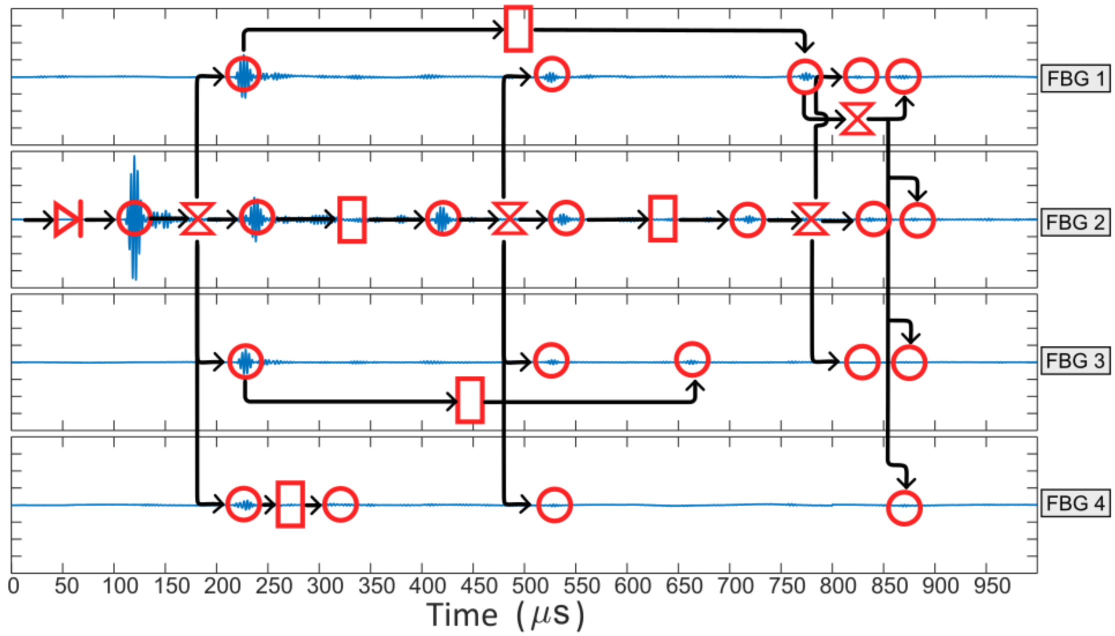

(c)

Figure 2.7 (a) The layout of where each event occurred along each FBG path in the experiment; (b) legend for flow chart; and (c) Measured signals with flowchart added to describe signal packets path of travel through the network.

2.3.2 Performance

We next model the coupler as an acoustic equivalent to a 2-by-2 passive optical or electromagnetic directional coupler [47]. While performance specifications of couplers are typically defined over a bandwidth, these experiments were only performed at the fixed frequency of 300 kHz, therefore all values are reported for the Hanning windowed signal centered at 300 kHz. Since the longitudinal mode is nondispersive below a few MHz in the SMOF, we can assume that the group velocity is constant for all frequencies within the wave packet [33], [38]. The energy of the propagating signal is stored along the SMOF as strain energy. The longitudinal mode can be approximated as a uniform axial strain across the fiber cross-section at the frequency used in these experiments [34]. The photodetector output is proportional to the axial strain induced by the longitudinal mode; therefore, the signal energy is proportional to the square of the photodetector signal amplitude [38].

The signal energy, *E*, is calculated across a series of discrete time steps as given in Equation 2.1 [38]. This expression is equivalent to the autocorrelation of the discrete-time signal. *X* corresponds to the entire series of measurements recorded by the FBG and *x* is the windowed subset of *X* that only encompasses the waveform of interest. n_{start} and n_{end} are the indices at the start and end of the windowed waveform. For these experiments, the entire incident waveform passed FBG 2 after 350 timesteps.

$$E = const * \sum_{n=n_{start}}^{n_{end}-1} |X(n)|^2 = const * \sum_{n=0}^{N_x-1} |x(n)|^2 \tag{2.1}$$

N_x was held constant at 350 for all calculations of the signal energy. Since the wave packet used in these experiments is nondispersive, the time needed for the entire signal packet to pass an FBG will not increase as the signal propagates along the fiber. Similarly, the ratio of energy between any two FBG measurements of equal number of time steps is equivalent to the ratio in power between the two signals. To determine the optimal placement of the n_{start} and n_{end} indexes a cross correlation between the incident waveform and the entire set of FBG measurements was performed.

The four branches of a 2-by-2 coupler were identified as the Transmitted, Input, Coupled and Isolated ports, labelled in Figure 6. Table 3 lists the signal power between the waveform measured by each FBG post signal-coupler. All power values in this table are normalized by P_{in}, or power of the incident waveform measured by FBG 2 before the signal-coupler interaction. The results are reported for all four trials of the experiments. The values listed for FBG 2 represent the acoustic energy that did not enter the coupler but rather reflected at the interface and remained along the input port. Each trial of the experiment is representative of the 4,096 individual PZT excitations. So, the average and standard deviation values listed in Table 3 reflect the 16,384 excitations that make up the 4 trials.

Table 2.3 Power measured at each FBG following first signal-coupler interaction.

	Power (P_{out}/P_{in})			
Sensor Port Name	FBG 1 Transmitted r_1	FBG 2 Input r_2	FBG 3 Coupled r_3	FBG 4 Isolated r_4
Trial 1	0.118	0.114	0.038	0.005
Trial 2	0.137	0.113	0.047	0.006
Trial 3	0.124	0.118	0.042	0.006
Trial 4	0.142	0.110	0.046	0.004
Average	0.130	0.113	0.043	0.005
STD	0.011	0.003	0.004	0.001

The performance of the CA coupler as a passive directional coupler will be broken up into two sections: the coupler's ability to transfer signal between waveguides and the losses incurred from the signal-coupler interaction. The loss analysis aims to identify what factors are limiting the overall performance. In the following section, we will evaluate the repeatability between the different experiments.

For a 2-by-2 directional coupler the transmitted and coupled ports represent the coupler outputs while the isolated and input ports are designated as potential inputs. In the case of the ideal coupler the signal power received by both output ports would be equal to incident signal, resulting in an overall 0 dB change across both outputs. The distribution of power between both output ports is called the coupling ratio (Equation 2.2) [47]. The coupling factor is the magnitude of the energy lost from the input port to the coupled port (FBG 2 to FBG 3) (Equation 2.3).

$$Coupling\ Ratio(dB) = 10\ \log\left(\frac{r_1 + r_3}{r_3}\right) \tag{2.2}$$

$$Coupling\ Factor\ (dB) = 10\ \log(r_3) \tag{2.3}$$

Directivity is a measure of a coupler's ability to isolate forward and reverse signals. It was calculated by comparing the undesired coupling at isolated port to what was received by the coupled port (Equation 2.4). In general, the higher the directivity of the coupler, the lower the overall measurement uncertainty. In the ideal case there would be no signal measured at the isolated port of the network, which would result in a directivity and isolation factors of -∞ dB. Isolation is a measure of the separation between both input ports (Equation 2.5).

$$Directivity\ (dB) = 10\ \log\left(\frac{r_3}{r_4}\right) \tag{2.4}$$

$$Isolation\ (dB) = 10\ \log(r_4) \tag{2.5}$$

Equations 2.2 through 2.5 were used to calculate the signal transference performance of the coupler for each trial. The results are listed in Table 2.4 below.

Table 2.4 Measured CA coupler signal transference performance.

	Output Power Dis (%)	**Coupling Ratio (dB)**	**Coupling Factor (dB)**	**Directivity (dB)**	**Isolation (dB)**
Trial 1	0.244	6.13	-14.18	-8.74	-22.9
Trial 2	0.255	5.94	-13.30	-8.78	-22.1
Trial 3	0.254	5.96	-13.77	-8.31	-22.1
Trial 4	0.244	6.12	-13.37	-11.2	-24.6
Average	0.249	6.04	-13.65	-9.26	-22.9
STD	0.00585	0.102	-0.41	-1.31	-1.17

The combination of all sources of losses that ultimately limit the signal transference to either output port of the network is known as excess losses (Equation 2.6). This expression of loss is unique as it includes the portion of the signals that are misdirected to the input ports of the coupler. In an ideal coupler the excess loss would be 0 dB and all signal power would reach either output port of the network.

$$Excess\ Losses\ (dB) = -10\log(r_1 + r_3) \tag{2.6}$$

Mainline insertion loss (Equation 2.7) is described by the power that is lost between the input and transmitted ports. This value represents a combination of the overall power that is lost due to signal transference to the other fiber and the other inherent losses of the directional coupler.

$$Mainline\ Insertion\ Loss\ (dB) = 10\log(r_1) \tag{2.7}$$

Attenuation losses considered the ratio of power received by all FBGs to determine the power lost from signal propagation through the coupler (Equation 2.8). Since both inputs ports are considered, the attenuation losses only represent the losses from both the SMOF and the CA coupler. The attenuation along a polyimide SMOF at 300 kHz is known at 1.303 dB/m [26]. When excluding the length of the coupler, the longest path between any two FBGs is 50.2 cm. This corresponds to 0.654 dB of attenuation due to propagation through the SMOF. Attenuation losses that exceed this value will be due to the propagation losses across the CA coupler's length.

$$Attenuation\ Loss\ (dB) = 10\log(r_1 + r_2 + r_3 + r_4) \tag{2.8}$$

The return loss is defined by acoustic power that reflected off the coupler and returned to FBG 2 (Equation 2.9). This loss stems from an abrupt impedance change that causes reflections when a signal attempts to enter the coupler.

$$Acoustic\ Return\ Loss\ (dB) = 10\log(r_2) \tag{2.9}$$

The loss-based performance specification of the coupler in terms of the previously stated equations for each trial were calculated and are shown below in Table 2.5.

Table 2.5 Measured performance losses of the coupler.

	Coupling Loss (dB)	**Insertion Loss (dB)**	**Excess Loss (dB)**	**Atten. Losses (dB)**	**Return Loss (dB)**
Trial 1	-0.170	-9.27	-8.05	-5.60	-9.44
Trial 2	-0.208	-8.64	-7.36	-5.19	-9.47
Trial 3	-0.186	-9.08	-7.81	-5.38	-9.29
Trial 4	-0.205	-8.47	-7.25	-5.21	-9.61
Average	-0.192	-8.86	-7.62	-5.35	-9.46
STD	0.018	0.371	0.376	0.19	0.132

In general, the results show that the acoustic coupler displayed levels of directivity and signal isolation comparable to other commercially available coupling devices. The CA coupler produced for this experiment displayed a coupling ratio of about 25:75, however, the CA coupler struggled to direct the acoustic signal to either output port of the coupler with an average excess loss of 7.62 dB. This level of loss indicates that on average 17.36% of the incident signal energy made it to either output port. Which leaves 82.64% of the incident energy unaccounted for, lost either due to attenuation across the coupler or unintentionally directing a portion of the signal to either input port. These levels of loss and input reflections exceed what was observed in the experiments that used a drop of CA as the coupler. Which was expected since their goal was to minimize the amount of CA used.

While typical commercially available optical couplers can achieve excess losses of less than 0.3 dB, they are fused core couplers that are precision manufactured to minimize loss. This level of performance was not expected from the acoustic coupler. In the case of the CA coupler tested we expected significant sources of signal loss that would not be present in the optical coupler. First, the CA polymer used for the coupler is not an ideal medium for propagating acoustic waves. Next, the longitudinal mode along the waveguide is prone to leakage which may have caused signal loss into the CA and the environment [48], [49]. Lastly, the coupler’s geometry was larger than the SMOF, and the change in diameter would likely cause an impedance mismatch at the SMOF-coupler interface. Despite the numerous potential sources of signal loss, the CA coupler functioned properly. The objective was to analyze the performance of a CA coupler like ones used in previous experiments. From these results useful information on mode interaction with the acoustic coupler was revealed. Analysis of the loss was used to identify potential improvements to the CA coupler design. In these regards the objectives were met and the CA coupler tested in this experiment was a success.

Return losses stem from impedance discontinuities between the waveguide and the coupler. As a result, a partial reflection of the signal occurs at boundary of the discontinuity. The larger the acoustic impedance mismatch between waveguide and couple, the larger the reflection. In this experiment we can assume this discontinuity exists between the boundary of the SMOF and the CA coupler. Waveguide impedance is dependent on both cross section and wave speed, both of which were influenced by the presence of the CA [50]. The return loss exhibited by a commercially available electromagnetic coupler typically ranges anywhere from 10 to 30 dB. The average return loss displayed by the CA coupler, 9.45 dB, just outside of this range. A return loss of this magnitude corresponds to a reflected intensity, R, of 0.1136. The relative change in impedance between the fiber waveguide and the coupler was then determined (Equation 10). The results show that the acoustic impedance through the coupler was 0.496 times smaller than the rest of the fiber network.

$$\frac{Z_2}{Z_1} = \frac{1-r}{1+r} \tag{2.10}$$

With performance limitations associated with misdirected signals discussed, the overall losses through the coupler will now be analyzed. The total attenuation loss calculation took the output of all four ports to measure the signal power lost following the signal-coupler interaction. Which left 70.78% of the incident signal power unaccounted for, or a -5.35 dB change in the incident power. This points to the attenuation across the CA coupler as the main contributor to the large levels of excess loss observed in the experiments. As stated previously, estimates on the propagation losses along the SMOF can only account for at most 0.654 dB of signal loss.

Leaving -4.70 dB of the overall loss due to the signal propagation through the 2.93 mm long CA coupler region. This corresponds to an attenuation coefficient of 1604 dB/m, over a thousand times larger than the bare SMOF. An increase in signal attenuation in this region was expected as CA is much softer than silica. However, such a drastic increase in signal attenuation across such a short component was not expected. The implications of these results will be further explored in the discussion.

Outside of the large losses due to attenuation the biggest limitation to the coupler's performance was its directivity. While the average directivity was measured at 9.26 dB many real-world couplers often require a minimum of 10 dB, however, ideally directivity would exceed 35 dB. Since the acoustic impedance of the coupler does not match the index along the SMOF signal reflections will occur as a signal enters and exits the coupler. Without proper separation of the forward and reverse signals, reflections that occur at the transmitted port can interfere with the coupled port. This would imply that some of the excess loss would stem from internal signal interference, however, it is not possible to gauge how much energy was lost to interference with the current experimental setup.

Highly directive couplers experience less variance in the coupled power level and are generally more accurate. However, the attenuation losses are the most prevalent performance limitation to the current coupler design. Going forward the directivity and isolation of the coupler should be monitored while the attenuation across the coupler is lowered.

2.3.3 Repeatability

In this section the repeatability of the coupler performance between different layouts of the fiber network. As the manufacturing process for the coupler is a manual one, the variability is expected to be higher than that of fused optical fiber couplers, which are fabricated with a precision process with in-line monitoring of the output coupling power. The standard deviation of the relative power received by the four ports (FBGs) and the coupler performance coefficients between the four trials are listed in Tables 2.3, 2.4 and 2.5. These tables demonstrate that the energy transferred was generally consistent across all four trials of the experiment. However, these results only consider the initial signal-coupler interaction and do not demonstrate the coupler's contribution to the variance. By monitoring repeatability across the entire measurement window, the stability of the secondary signal-coupler interactions can be considered.

The first repeatability analysis modeled the standard deviation of each FBG strain measurement at each time step. The deviation in measured strain amplitude was calculated and plotted against time, seen in Figure 2.8. This analysis was used to identify when the most variance occurred following PZT excitation. As well as compare the prominence of deviations to the measurement resolution of the FBG.

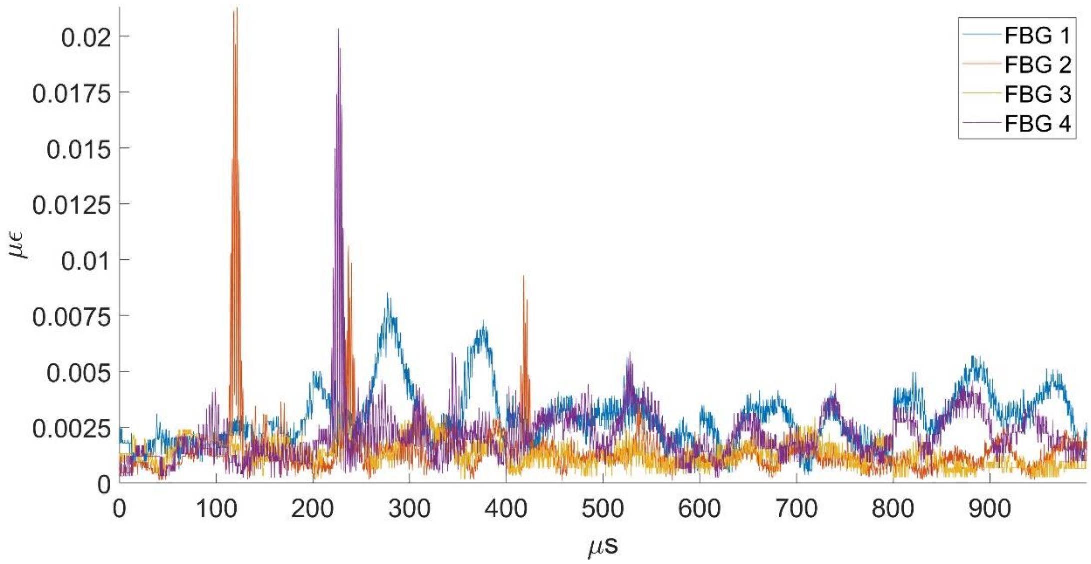

Figure 2.8 Standard Deviation in Strain measurement between all 4 trials for each FBG.

Figure 2.8 shows that the largest spike in deviation occurred at FBG 2 before the first signal-coupler interaction. The magnitude of the deviation spikes that followed steadily diminished as the signal interacted with the coupler. Suggesting the largest source of instability between each trial stemmed from external factors and not the coupler itself. Each spike in variance along the FBG 2 measurements occurred when a signal packet was passing FBG 2. The width of each spike covered a period roughly the same duration as the initial wavelet that entered the coupler.

Aside from a single spike along FBG 4, Figure 2.8 also showed that the other FBGs did not display the same defined spikes in variance that were observed along FBG 2. Instead, the variance between each trail seemed to drift around what is believed to be the noise floor of each sensor. This value is tied to the measurement resolution of each FBG which is affected by the FBG's reflected spectrum, and other equipment-based factors. No two FBGs share the same reflected spectrum so the measurement resolution varied slightly between each sensor. The noise floor of each sensor is most clearly displayed within the first 100 μs following PZT excitation, as there is no strain along any FBG.

Unfortunately, a direct comparison of each timestep cannot accurately report deviations in the shape of the waveform. A misalignment of a single timestep in any trial would result in the comparison of dissimilar waveform features. Both time and envelope shape must be considered simultaneously to determine the coupler's ability to repeatability interact with the entire waveform.

For discrete-time signals, a cross correlation will determine the similarity between two time series using a sliding dot product. This process returns similarity as a function of lag; or the amount of time steps one series was displaced before the dot product was performed. In section 2.3.2 the cross correlation was used to identify the optimal boundaries for the relative power calculation. Here, the cross correlation is performed for all positive values of lag. In such a way that the waveform surrounding an FBG is reflected in each time step. Thus, preventing the potential timing issues observed with the original deviation analysis.

$$\hat{R}_{x,Y}(m) = \sum_{n=0}^{N-m-1} x_{n+m} Y_n^* \tag{2.11}$$

The cross-correlation between two time series *x* and *Y* as a function of the lag, *m* (Equation 2.11). Where, *Y* is the entire set of measurements recorded by any FBG, and *N* is the total length of the set. The series *x* is the windowed subset of the FBG 2 measurements. Including only the 350 individual measurements that make up the initial signal entering the coupler. The rest of the series *x* is padded with zeros so that it is the same length as the series *Y*. This way the cross correlation only compares a segment of *Y* to the entire incident signal.

Since lag is equal to the sampling period of the measurements, in this case (m = 0.2 μs). The lag can be converted back into a measure of time. Equation 2.11 was used on all 4 sets of FBG measurements across all four trials of the experiment. For every time step the correlation values were normalized by the signal energy of the initial waveform, determined with Equation 2.1. The normalized correlation values represent the overall difference in waveform amplitude as a ratio. By squaring the normalized values for each timestep the results will now be expressed in terms of an energy difference. As expected, a maximum value of 1 occurred along FBG 2 when the initial waveform was measured. Since the cross-correlation in this location will be equivalent to the normalization factor.

Point by point deviation calculations were no longer as sensitive to temporal inconsistencies since each value produced by the cross correlation is representative of the entire waveform passing the FBG. The deviation in energy content surrounding each FBG at each time step was calculated across the four trials of the experiment, seen in Figure 2.9. It's important to point out that the largest spike in variance observed in Figure 2.8 was due to the incident signal. Because the initial signal is used for normalization in this analysis, deviations in the initial waveform cannot be observed in Figure 2.9.

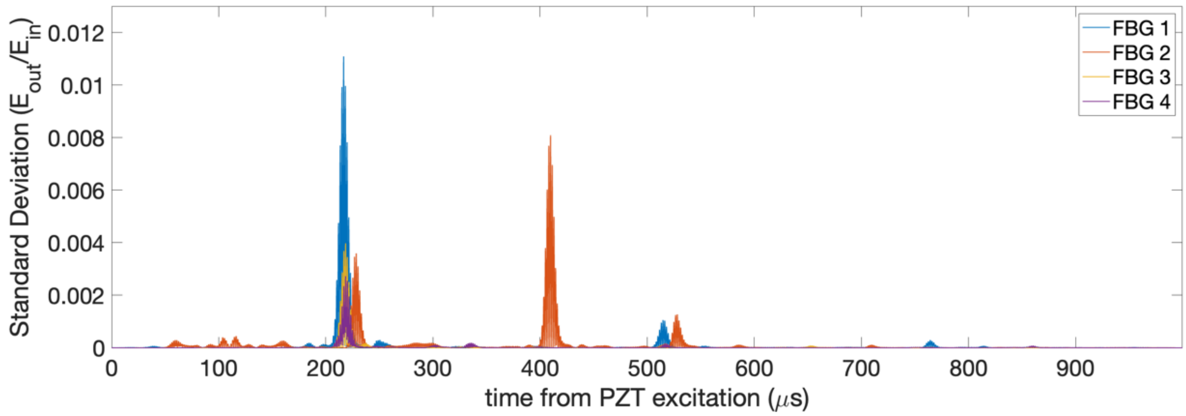

Figure 2.9 The standard deviation of relative waveform energy at each FBG following PZT excitation.

Figure 2.9 displays the variance in the energy measured by the FBGs as the signals propagated through the fiber network. The first set of peaks observed are among the largest and correspond to the first signal coupler interaction. Even then the relative energy content measured by FBG 1 only varied 1% across the four trials. The magnitude of these peaks also closely matches the standard deviation reported in Table 2.3. Indicating that the calculation successfully modeled the variance in signal energy. Figure 2.9 also shows that following the 1st signal coupler interaction, the peak deviation measured by FBG 2 nearly doubled. The waveform passing FBG 2 at this point in time corresponds to the reflection off the CA thin film bond. Which again indicates that the differences between each trial of the experiment primarily stemmed from the CA thin film. This is also supported when looking at the deviations across the initial signals. The signal energy for each of the initial waveforms was calculated and then normalized by the average energy. The deviation in relative energy across the four initial waveforms was measured at 7.7%. The peak deviation across every FBG measurement after the 1st signal coupler interaction is not close to this value even when summed. Meaning deviations decreased following an interaction with the coupler. This shows that while there were slight variances between each trial of the experiment the acoustic coupler distributed the signal energy throughout the fiber network very repeatably. The repeatability analysis demonstrated the coupler performance is very consistent across many PZT excitations, and that the largest source of trial-to-trial variance stemmed from the plate-to-fiber CA thin film bond.

2.4 Discussion

The results of the following experiments demonstrate the performance and consistency of a mold based adhesive coupling device. Fabricating stable acoustic coupler for is straightforward and inexpensive with room to improve the design. In this discussion theoretical predictions pertaining to mode interaction with an acoustic coupler will be analyzed and compared to the results measured in the CA coupler used in this experiment.

It is important to point out that for optical couplers, signal coupling occurs through evanescent fields generated in the shared cladding region of both waveguides. The reliance on evanescent fields leaves the optical mode completely confined to the core of the SMOF, which generate evanescent waves in the surrounding cladding. This allows for the manufacture of optical couplers with very low losses as there are virtually no discontinuities across the optical coupler and net energy flow through the cladding is zero. This method of signal transference is described by coupled mode theory. The theoretical predictions on acoustic coupling that are based on coupled mode theory first assume that the two cores are well separated.

For acoustic waveguides, two cores can be considered well separated if the distance between their center axes, d, is $>> \lambda$ [37]. Where λ is the wavelength of the signal. For two standard 0.15 mm ⌀ polyimide coated SMOFs that are directly bonded to one another, a 300 kHz acoustic signal will have a wavelength of 17 mm. If the lack of separation between the waveguides and poor mode confinement from leakage are considered, there is a strong possibility that the mechanism of acoustic signal transfer in this case is not based on evanescence.

The large attenuation and return losses observed from the tested coupler support this possibility since mode propagation was heavily affected by the presence of the CA. Indicating that the mode was not confined to the fiber waveguide but rather distributed across the entire coupler cross section. This is conclusion is supported by theory which predicts that at a frequency of 300 kHz the acoustic properties of the coupler should be some combination of the SMOF and CA's properties [34]. Given this assumption one could conclude that the CA contributed far more to the coupler's acoustic properties than the SMOF. When the maximum width of the coupler, 457.2 μm, was compared to the 125 μm diameter SMOF it became apparent that the coupler was mostly made of adhesive. Indicating a need to limit the amount of CA used in the coupler. This way, the favorable acoustic properties of silica are more prevalent in the final coupler. These results may also be achieved with the inclusion of additives in the CA to control the acoustic properties of the adhesive.

While there are many adhesives with acoustic properties superior to CA, the fixture time and cost still make CA an attractive material to use for fabricating acoustic couplers in field. To improve the design of the coupler without changing the CA adhesive used, the results point to decreasing the size of the coupler's cross section. Limiting the presence of adhesive in the design would reduce the overall cross section, which results in better impedance matching between the fiber waveguide and the coupler. Fabricating smaller couplers by reducing the size of the mold cavity is not a realistic option, as proper mold release was already a significant challenge with the current dimensions. Thus, further refining the design of the acoustic coupler would involve developing a new fabrication process, capable of producing smaller cross section couplers. Once the coupler's fabrication is enhanced, performance can be further improved by exploring various ceramic additives that can be used to control the acoustic properties of CA. With this the final impedance of the coupler can be tailored for each application and overall limit the signal loss through the coupler region.

2.5 Conclusion

A CA based acoustic signal coupling device, suited for field applications was successfully demonstrated. The acoustic coupler was fabricated with a stainless-steel mold which joined two SMOF. With FBGs along all four ports of the network mode propagation through the coupler was observed. The signals interaction with the coupler was determined to be stable and path traveled through the said network repeatable. The performance of the CA couple was then gauged as a directional coupling device. Despite the multiple significant sources of signal loss identified, the coupler's overall performance exceeded expectations. While the mold was specifically designed to limit the cross-section of the coupler, an analysis of the performance losses indicated that coupler cross-section was still too large. This contributed to reflections at the signal-coupler interface and introduced additional losses from the CA. Future attempts to refine the CA coupler design will require further minimization of the cross section that cannot be achieved with the mold. Additionally, performance could also be improved by either replacing or using additives with the CA. Modifying the adhesive so that it's acoustic properties better match the SMOF will minimize the impedance mismatch and limit the attenuation losses.

2.6 Acknowledgements

The authors thank the Office of Naval Research (ONR) (N00014-20-1-2583) for support of this research.

CHAPTER 3

Laser Doppler Vibrometry Measurements of Acoustic Attenuation in Optical Fiber Waveguides

Fiber Bragg grating (FBG) sensors have been widely applied for structural health monitoring applications. In some applications, remote bonding of the optical fiber is applied, where ultrasonic waves are coupled from the structure to the optical fiber and propagated along the fiber to the FBG sensor. The distance that this signal can propagate along the optical fiber without decaying below a threshold value can be critical to the area of the structure that can be monitored per sensor. In this paper we develop a method to measure the acoustic mode attenuation of fiber waveguides based on laser Doppler vibrometry (LDV) that is independent of the fiber type. In order to validate the method, we compare attenuation measurements on single-mode optical fibers using both the LDV and FBG sensor methods. Once the method is validated, experimental measurements of different coated and uncoated optical fibers are performed to quantify the role of fiber diameter in on the attenuation coefficient. As the radius of the waveguide decreased the signal attenuation increased exponentially.

3.1 Introduction

In structural health monitoring (SHM) guided wave techniques such as the ultrasonic pitch catch method are popular due to their robust damage detection capabilities [31]. The effectiveness and spatial coverage of this technique is reliant on the implementation of high sensitivity sensors to detect the guided waveform. While piezo-electric transducers (PZTs) offer excellent sensitivity and are widely used to generate ultrasonic waves in SHM, PZTs are difficult to integrate preexisting systems and the brittle nature of ceramics limits the life span of the sensor [1]. Fiber Bragg grating (FBG) sensors offer a more durable sensor in corrosive environments and offer the potential to multiplex a large number of sensors in a single fiber, therefore covering a large surface area with a single FBG interrogator [13].

However, the sensitivity of a FBG directly bonded to a structure is smaller than a comparable PZT sensor, due to its small contact area with the structure. This base sensitivity can be enhanced through methods such as the remote bonding technique which relies on coupling the symmetric (S_0) and anti-symmetric (A_0) Lamb waves from the structure into longitudinal L_{01} modes along the optical fiber [26], as shown in Figure 3.1. The L_{01} mode is then detected with the FBG at a location remote from the structure. In this case, the FBG interacts with the longitudinal wave along the fiber rather than the Lamb waves in the structure, resulting in a larger signal output [26], [31], [40] .

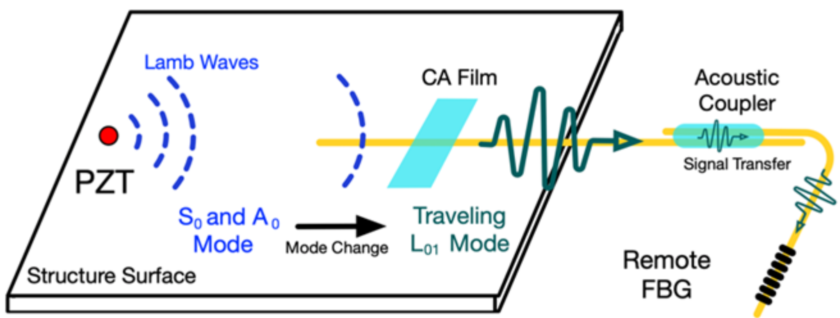

Figure 3.1 Coupling of Lamb waves to optical fiber into the L_{01} mode in the remote bonded FBG configuration.

Additionally, the ultrasonic L_{01} modes can be transferred from one fiber to another through an acoustic coupler [30], [41]. Coupling between fibers opens the possibility that the fiber waveguide bonded to the structure does not need to be standard single-mode optical fiber to enable writing of FBGs in the fiber. Kim et al. [30] demonstrated acoustic couplers to transfer the L01 mode from cylindrical waveguides of various materials and sizes to an optical fiber.

However, with the possibility of expanding the potential geometry and material for the fiber waveguide from the structure to the acoustic coupler, it is important to predict the attenuation of the acoustic mode as a function of the waveguide material and geometry. Researchers have investigated the theoretical acoustic mode propagation at frequencies up to a few MHz in optical fibers to predict the dispersion curve of the L_{01} mode [31]. However, these studies did not predict the attenuation coefficient of the mode, as it depends on the environment surrounding the optical fiber and imperfections in the fiber. The distance that the acoustic signal can propagate along the optical fiber without decaying below a threshold value can be critical to the area of the structure that can be monitored per sensor.

For acoustic propagation along the fiber waveguide, there are two sources of energy loss that determine the overall attenuation coefficient [36], [40], [49]. The first, internal damping, is inherent to the material that makes up the waveguide and is largely determined by the thermal properties of the material. The second, radial mode leakage, represents the acoustic energy that leaks out of the waveguide and is lost to the environment. The distribution of optical index refraction in the fiber cross-section confines lightwaves near the core region. However, the ultrasonic modes are distributed more widely throughout the fiber cross-section. This is due to the fact that the ultrasonic mode is at a much longer wavelength (on the order of 10 mm) and the lack of a gradient in acoustic properties across the cross-section. Therefore the radial mode leakage is much stronger for the ultrasonic modes and the ultrasonic mode is much more sensitive to the surrounding environment and the coating on the optical fiber. [26].

Experimental measurements of attenuation for ultrasonic L_{01} modes in optical fibers have been previously performed. Wee et al [26] measured the acoustic attenuation of a single-mode optical fiber using multiple FBG sensors. Lee and Tsuda [31] performed the same measurement using PZT sensors glued to the end of the fiber. These measurement techniques are limited to cases where the FBG sensors can be written into the waveguides or a coupling to actuators and detectors is easily available. In this paper we develop a method to measure the acoustic mode attenuation of fiber waveguides based on laser Doppler vibrometry (LDV) that is independent of the fiber type. In order to validate the method, we compare attenuation measurements on single-mode optical fibers using both the LDV and FBG sensor methods. Once the method is validated, experimental measurements of different coated and uncoated optical fibers are performed to quantify the role of fiber diameter in on the attenuation coefficient.

3.2 Attenuation Measurement Methods

3.2.1 Standard FBG Attenuation Measurement

The first attenuation measurements were performed using FBG sensors in the core of the optical fiber. Fig. 2 shows the setup of the FBG based method for measuring attenuation. Lamb waves were generated in an aluminum plate by exciting the PZT actuator with a 5.5 cycle 300 kHz Hanning windowed waveform. The waveform was generated by an arbitrary waveform generator (AWG) and signal amplifier. All measurements were performed at the same input frequency since the frequency dependency of the attenuation coefficient is beyond the scope of this paper. The 6061 aluminum plate has dimensions 609.6 mm by 609.6 mm and thickness of 0.8 mm. The edges of the plate were lined with Dynamat® damping material to prevent signal reflections from occurring at the edges of the plate. The optical fiber was bonded to the plate by a 2 cm by 1 cm thin film of cyanoacrylate (CA). It was previously demonstrated that CA adhesive well transfers Lamb waves in the structure to traveling waves in the optical fiber through the adhesive bond [30], [41]. The film was placed 10 cm from the PZT to allow the S_0 and A_0 modes to sufficiently separate prior to arriving at the bond.

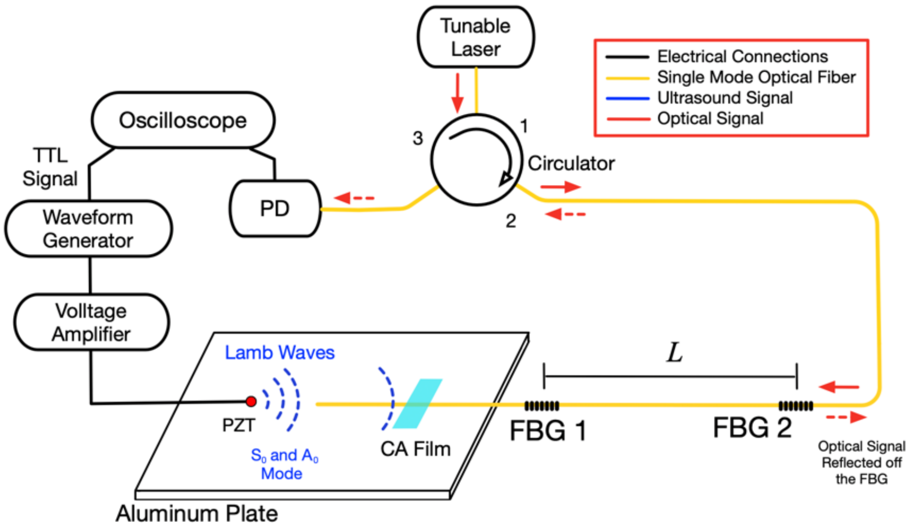

Figure 3.2 Setup of the FBG based attenuation measurement.

The Bragg wavelengths for FBG 1 and FBG 2 are 1568 nm and 1572 nm respectively. The dynamic strain on the FBGs were extracted using an edge filtering method with the output of a tunable laser set to the midpoint of the rising edge of the FBG reflected spectrum. The tunable laser output was passed through an optical circulator to the FBG sensors. The reflected lightwaves from the FBGs passed through the circulator to a photodetector. The input waveform from the wave generator and the output waveform measured by the photodetector were recorded by the oscilloscope. The two signals were time synchronized using the transistor-transistor logic (TTL) signal from the AWG was used as a trigger signal. The collected waveforms were averaged over 4096 measurements with a 10 ms burst time to limit the noise in the measurements. As will be discussed in the results, the radial leakage of energy out of the fiber is highly sensitive to the surrounding environment, therefore the high number of averages were performed.

Assuming a constant attenuation along the fiber, the attenuation of the acoustic signal amplitude as the L_{01} mode travels the distance L from FBG 1 to FBG 2 can be modeled by Equation 3.1.

$$A_2 = A_1 \ \exp(-L\,\alpha) \tag{3.1}$$

$$-\left(\frac{1}{L}\right)\ln\left(\frac{A_2}{A_1}\right) = \alpha \tag{3.2}$$

where α is acoustic attenuation per meter along the optical fiber, A_1 and A_2 are the signal amplitudes measured at FBGs 1 and 2, and L is the length between the two FBGs. As the wave velocity of the L_{01} mode in the optical fiber is known from previous experiments [36], the distance L could be accurately determined. The attenuation coefficient α was then calculated from Equation 3.2 for each measurement.

To minimize the effect of measurement noise in the calculation of α, the amplitude decay was calculated using the cross correlation, $\hat{E}_{xy}$. All the amplitudes measured across the time window by FBG 1 and FBG 2 were represented by x and y respectively. Where x_n and y_n represent the n^{th} amplitude measurement in their respective sets, in order of when they were recorded so that $n = 1\ldots\ldots N$.

$$\hat{E}_{xy}(m) = \sum_{n=0}^{N-m-1} x_{n+m}\, y_n \tag{3.3}$$

The maximum value of the cross correlation was normalized to the auto-correlation of the signal at FBG 1 to itself, $\hat{E}_{xx}(0)$,

$$\hat{E}_{xx}(0) = \sum_{n=0}^{N-1} (x_n)^2 \tag{3.4}$$

to determine the change in amplitude across the overall wave packet.

$$\frac{A_2}{A_1} = \frac{max\left(\hat{E}_{xy}(m)\right)}{\hat{E}_{xx}(0)} \tag{3.5}$$

3.2.2 LDV Attenuation Measurement Methods

In the second method for measuring the attenuation of the L_{01} mode in an optical fiber waveguide, the L_{01} mode is launched into the fiber in the same manner as described previously, however the mode amplitude is measured using a laser Doppler vibrometer (LDV) focused on the outer surface of the fiber. The setup for this method is shown in Figure 3.3. The LDV is aligned above a point on the optical fiber and the velocity of the fiber surface in the axial (x) direction is measured. The challenge to this measurement, particularly for small fiber diameters, is that the measured surface displacement is also highly sensitive to small displacements of the optical fiber since these would change the relative angle between the curved fiber surface and the LDV.

For this reason, a 3D LDV with the three beams integrated into the same sensor head and an extremely small laser spot size (4 µm) was used for the measurement (MSA-100-3D, Polytec GmbH). The aluminum plate that is mounted on a precision XY stage which moves the sample under the sensor head so different locations can be scanned. The scan portion of the fiber is spray-coated with a layer of CRC Weld Check® to reduce the reflectivity of the aluminum plate and so light scattering from the surface is uniform. Figure 3.4 shows the aluminum plate placed under the 3D LDV sensor head and the scan point along the center line of the optical fiber. At each scan point, the 3D LDV collected the ultrasonic wave axial velocity with a sampling frequency of 6.25 MHz. The TTL signal from the AWG was used to average the measurement over 1200 burst periods. The XY precision stage then translated the specimen from scan point to scan point with the precision of ± 0.5 μm, until all points are scanned. The spatial resolution of the LDV method is dependent on the degree of precision we can determine each of the scan points' location. In this experiment the resolution was determined by the XY stage repeatability and the laser spot size.

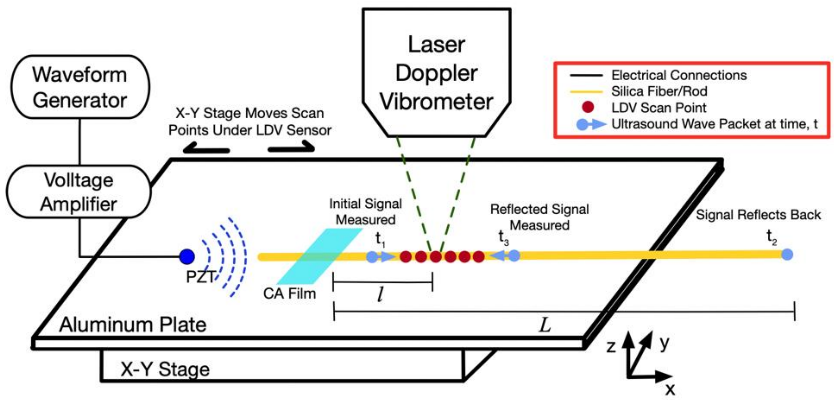

Figure 3.3 Setup of the LDV based attenuation measurement.

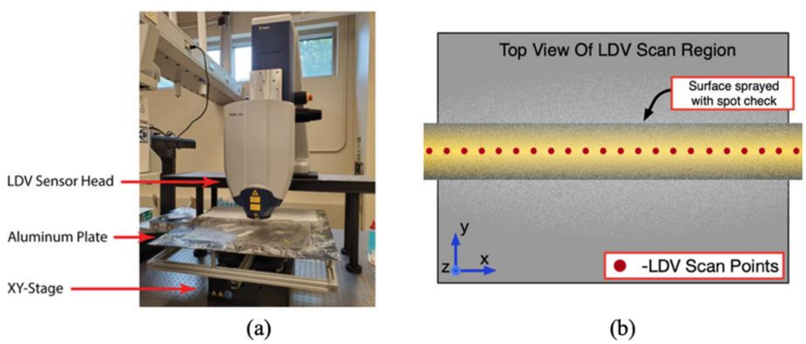

Figure 3.4 (a) Photograph of LDV setup and (b) schematic of silica rod with scan points indicated.

The advantage of using the 3D LDV to measure optical fiber acoustic attenuation is that writing of a FBG in the optical fiber is not required, therefore a larger variety of optical fibers could be used to extract the Lamb wave from the plate. However, the disadvantage is that the measurement is performed on the outer surface of the fiber, rather than in the fiber core. As the acoustic mode is distributed throughout the fiber cross-section, the surface velocities can be used to measure the waveform. In addition, the three beams of the LDV must be aligned on the highly curved surface of the optical fiber. A small movement of the fiber relative to the LDV system changes the angle of the laser reflections and therefore can create an apparent amplitude change for the ultrasonic mode. This noise source became significant when the plate was displaced by the translation stage between measurements.

To reduce this effect, the measurement approach was modified, as shown in Figure 3.3, such that the L_{01} mode was measured at one scan point, then propagated along the optical fiber and was reflected off a cleaved end of the optical fiber. The wave then propagated along the optical fiber to the original scan point and was measured a second time by the LDV. The location and travel direction of the ultrasonic mode as it moved through the experiment can be seen in Figure 3.3. At t1 the L_{01} mode coupled from the plate initially passes underneath the LDV sensor head and is measured. Sometime later at t_2 the wave packet reaching the end of the fiber waveguide reflects. Finally, at t_3 the wave packet returns underneath the LDV sensor head where the signal is measured again. The attenuation is found by comparing the amplitudes of the wavelets measured at t_1 and t_3. Once the ratio of amplitude loss was determined via the normalized cross correlation the length the signal traveled was calculated. A single scan point was placed right at the edge of the CA film and served to correlate the X-Y stage coordinate space with a location along the optical fiber. The distance between this point and each scan point was subtracted from the total length of the sample, the remaining length multiplied by two represented the total length the wave packet traveled between times t_1 and t_3.

The LDV system therefore measured the L_{01} mode twice at the same point on the optical fiber, from which the attenuation coefficient could be calculated. Since the fiber did not have to be translated relative to the LDV system, the error due to reflection angle was significantly reduced. A second benefit is that the distance to the cleaved end of the fiber could be arbitrarily far beyond the translation limits of the stage, increasing the travel distance of the L_{01} mode between the two measurements. This increased the accuracy of the attenuation measurements, since the attenuation per meter is small.

This modification relies on the large impedance mismatch between silica and air, which means that a negligible amount of energy is lost during the reflection of the L_{01} mode from the cleaved end of the fiber. At normal incidence theoretically 99.8% of all acoustic energy should reflect back into the silica, based on the reflected power.

$$R = \left(\frac{Z_{silica} - Z_{air}}{Z_{silica} + Z_{air}}\right)^2 \tag{3.6}$$

with Z_{air} = 0.4 x 103 kg/m2s and Z_{silica} = 1.3 x 107 kg/m2s [51].

3.3 Attenuation Measurement Results

3.3.1 Validation of LDV Attenuation Measurement

Attenuation measurements were first performed on the same type of single-mode optical fiber using both the FBG and LDV methods, in order to validate the LDV approach. This fiber was also the same fiber type used for the previous attenuation measurements with two bond locations and one FBG, presented in Wee et al [26]. The silica fiber is 125 µm in diameter with a 5 µm thick polyimide coating. Since the attenuation coefficient of the acoustic modes is also highly dependent on the surrounding environmental conditions, the same FBG test was repeated

49 times, over the period of approximately one month, to understand the variability of the measurements.

Figure 3.5(a) plots a histogram of the measured attenuation coefficients for these experiments. An average attenuation value of 0.1372 m-1 and a standard deviation of 0.053 m-1 were calculated. The first observation from the histogram is the large variability in the data, leading to the large standard deviation value. As a result of the large standard deviation, some measurements resulted in a negative attenuation value which is not physically possible. However, the mean value is within one standard deviation of the value previously reported by Wee et al. [26], included in Table 3.1 summarizing the results. These results highlight the difficulty in measuring the attenuation of L_{01} modes in the optical fiber due to the large amount of radial leakage and therefore the strong sensitivity of the loss to the surrounding environment. It is also important to point out that Wee et al. [26] only performed a few measurements of the attenuation coefficient and did not consider the repeatability of the measurement.

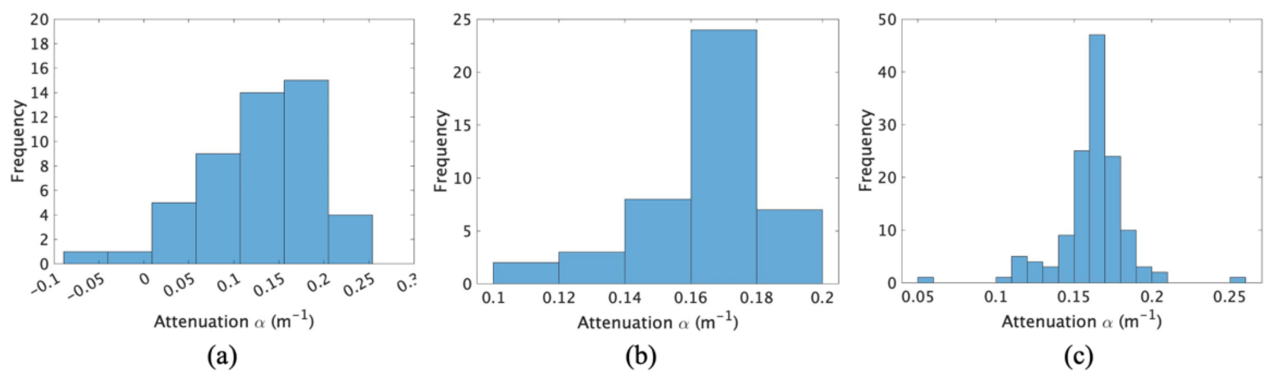

Figure 3.5 Histograms that show distribution of the measured attenuation coefficients for (a) 44 measurements with the FBG method and (b) the 135 measurements taken with the LDV method.

Table 3.1 Measured L_{01} attenuation coefficients for coated, single-mode optical fiber.

Method	Average Attenuation (m^{-1})	Average Attenuation (dB/m)	Standard Deviation (m^{-1})	Standard Deviation (dB/m)
FBG	0.1372	1.192	0.053	0.462
LDV (44)	0.1628	1.414	0.018	0.153
LDV (135)	0.1619	1.406	0.021	0.182
Wee et al [26]	0.15	1.303	-	-

The experiments were then repeated on the same fiber type using the LDV method for 44 samples to create a set of measurements the approximate size of the FBG set. Figure 3.5(b) plots a histogram of the measured attenuation coefficients for these experiments. An average attenuation value of 0.1628 m-1 and a standard deviation of 0.018 m-1 were calculated. The average attenuation value was within one standard deviation of the FBG method, indicating that the LDV data can be used to calculate the attenuation of L_{01} mode. The standard deviation across the entire data set was also less than half of the FBG counterpart, which can be seen in Figure 3.5 (b). The smaller variance of the data also meant that negative attenuation values were not calculated in the data. Because the data can be collected from multiple points along the fiber, collecting multiple data sets can be done much quicker and 135 measurements were then collected. An average attenuation value of 0.1619 m-1 and a standard deviation of 0.021 m-1 were calculated, only slightly different values compared to the smaller sample set. The histogram for these measurements is plotted in Figure 3.5 (c).

The higher degree of agreement across all measurements initially indicates the LDV method has a higher degree of precision than the FBG method. However, the LDV measurements were collected in a single day, due to the rapid data collection time. Therefore, the variations in environmental conditions present for the FBG measurements were not a factor for the LDV measurements. Therefore, we can conservatively conclude that the LDV measurements are at least as accurate as the FBG measurements, and that the curvature of the optical fiber did not create significant noise in the measurements.

3.3.2 Attenuation Coefficient of Silica Waveguides of Different Diameters

The LDV method was then applied to measure the attenuation in silica fibers of different diameters to evaluate the effect of fiber diameter on the attenuation. Measurements were performed on commercially available uncoated silica fibers and polyimide coated optical fibers. For the uncoated optical fibers, optical fibers with diameters of 125, 200, 400, and 600 μm and acrylate coatings were purchased from Thorlabs. The acrylate coating was removed with an acetone wash. Pure silica rods with diameters of 1, 1.75, 1.95, and 3 mm were also obtained from Technical Glass Products to study large fiber diameters. Polyimide coated optical fibers with diameters of 125, 400, and 600 μm were also purchased from Thorlabs for comparison with some of the uncoated samples. Each of the fibers was bonded to the plate as outlined in section 3.2.2 and 10 fiber samples were tested for each fiber type.

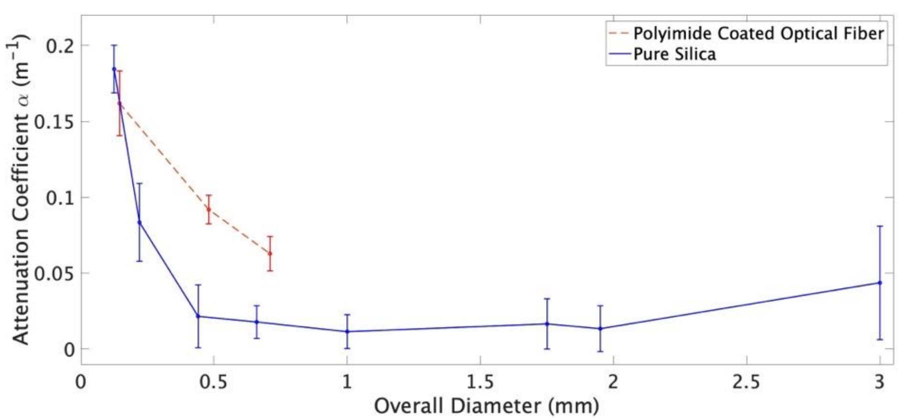

Figure 3.6 Attenuation coefficient of silica waveguides with and without polyimide coating.

The measurements of attenuation for each of the fiber types are plotted in Figure 3.6. The range of attenuation coefficient measurements for each fiber type are shown as error bars in the same plot. For the uncoated fiber, the attenuation coefficient exponentially decreased as the diameter increased until approximately 600 µm, after which the attenuation coefficient was roughly constant. An increase was observed for the 3000 µum diameter fiber, however the surface velocities measured by the LDV was significantly lower for this case. As a result, the initial particle velocity at the surface of the 3 mm rod was not much larger than the baseline noise associated with the LDV and the signal to noise was significantly lower, as can be seen in the error bars for this diameter in Figure 3.6. This could be due to the overall distribution of acoustic energy within the large diameter cross section and the difficulty in coupling a significant amount of energy from the plate into the rod.

The exceedingly low attenuation measured across the larger diameters show that the main source of acoustic signal loss along a conventional 125 µm single mode optical fiber is mode leakage into the environment. A 3 dB acoustic signal loss across a single mode optical fiber would occur across a 2.02 m segment while the same loss would occur across a 37.24 m segment of a 1 mm silica rod.

A similar trend in the attenuation with fiber diameter were observed by Drescher-Krasicka et al. [48] who evaluated radial mode leakage in a cylindrical waveguide with a Silicon Carbide (SiC) core and Aluminum cladding. As the radius of the SiC core decreased the acoustic energy leaking from the core increased. In the case of the optical fiber studied in this work, the entire silica region acts as the core and the surrounding air acts as an infinite cladding. There is therefore a much larger mismatch in acoustic properties of the silica core and the air cladding than that of the fiber studied by Eva Drescher-Krasicka et al. [48].

While fewer diameters were available for the polyimide coated optical fiber, the attenuation for those diameters showed the same trend as for the uncoated fibers. Overall, the attenuation along the polyimide coated samples was higher than for the uncoated fibers. This was expected since the acoustic properties of polyimide are not favorable compared to silica and coated fiber should be some combination of the properties of the coating and core [34]. For the two smallest fibers, the polyimide coated fiber had a lower attenuation value, however both measurements are within the error limits of each other, therefore, it is difficult to draw a conclusion as to whether there is a real difference in attenuation coefficient.

3.4 Conclusions

Laser Doppler vibrometry can be effectively used to measure the attenuation coefficients for acoustic modes propagating along an optical fiber. Due to the large wavelength of acoustic modes, as compared to the fiber diameter, the mode is spread throughout the fiber cross-section and can be detected on the outer surface of the fiber. The results of this work demonstrate that the LDV method produced attenuation coefficients comparable with equivalent measurements using FBG sensors. The LDV method enables the measurement of acoustic properties in a larger set of optical fiber types than those into which FBG sensors can be written. This capability could potentially benefit fiber sensing applications which use propagating acoustic modes in these fibers.

3.5 Acknowledgement

The authors thank the Office of Naval Research (ONR) (N00014-20-1-2583) for support of this research.

CHAPTER 4

Enhancing Cyanoacrylate Acoustic Coupler Performance through Flow Coating Fabrication

Optical fibers have found a secondary use as acoustic waveguides in the field of SHM, capable of guiding ultrasonic information in the form of the L_{01} mode. Acoustic couplers offer the ability to extend the usefulness of this utility by providing a passive means of transferring the signal between waveguides. While coupling devices can be fabricated inexpensively with Cyanoacrylate (CA) the performance has been limited by large insertion and return losses. In this experiment an acetone-based CA solution was used to fabricate the acoustic couplers through a flow-coating process. Capillary action between two optical fibers minimized the adhesive deposited and created a uniform coupler shape. Overall, the flow coating method was shown to enhance signal transference and minimize losses when compared to previously studied CA couplers. In addition, demonstrated that flow coating can produce a coupler with a tapered boundary, minimizing return losses. A second experiment monitored the performance of two couplers as the length of the coupler was decreased. Aside from the loss component the coupler's length displayed no discernible effect on behavior. Displaying uniform power splitting across all output ports of the coupler.

4.1 Introduction

Fiber Bragg Gratings (FBGs) are commonly used for acoustic sensing. The ability to multiplex signals makes them attractive options for damage detection applications in the field of Structural Health Monitoring (SHM) [13], [22]. Acoustic vibrations induce strain along the FBG, the magnitude of strain is measured by the corresponding shift to the FBG's characteristic Bragg wavelength. The use of spectral based FBG interrogation lacks sufficient sampling speeds and cannot track the Bragg wavelength shift with enough precision for use in ultrasonic sensing. Limiting the use of typical FBG interrogators for static low frequency vibrations [17]. Instead, intensity based FBG demodulation techniques such as the edge filtering configuration are used to measure vibrations in the ultrasound frequency range [12], [25]. However, the ability to use wavelength division to multiplex the optical signals from the FBGs is lost alongside the spectral component.

By utilizing the single mode optical fiber (SMOF) as an acoustic waveguide signal multiplexing can be performed in the acoustic domain. This requires the secondary fibers to act as a guide directing the acoustic signals from any point of interest to another fiber which houses an FBG. A diagram of this setup can be seen in Figure 4.1. Mode propagation along a single mode optical fiber (SMOF) has already been utilized as a means of directing acoustic signals [28], [29]. When this is applied to SHM the Lamb waves from the surface of the structure are coupled as the traveling extensional L_{01} mode along the fiber. The traveling mode is then guided along the fiber waveguide. Wee et al. [26] demonstrated how mode propagation can be applied in sensing applications with the remote bonding technique. They reported that amplitude measured by FBG increased when the FBG was not bonded directly to the structure. Demonstrating that measuring the L_{01} mode with the FBG was preferable to directly measuring the Lamb waves [26], [52], [53].

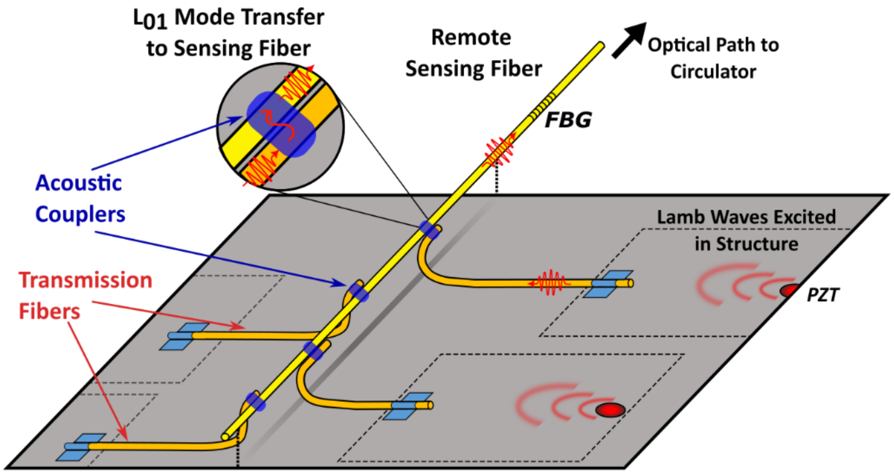

Figure 4.1 Potential distributed sensing network utilizing acoustic multiplexing.

To perform multiplexing with acoustic signals, passive coupling devices are needed to combine signals along separate waveguides to a single fiber. In this configuration every individual waveguide will provide sensing at the locations where they are bonded to the structure, reducing the need for more than one FBG sensor.

While theoretically a fused couplers should be the ideal for signal transference Mathews et al. reported large return and insertion losses. In addition, fused couplers are brittle and cannot be undone making the fabrication technique not practical for SHM applications. Recently, Kim et al. [39] demonstrated an alternate approach by simply adhesively bonding two optical fibers to one another. Since only the acoustic signals needed to be transferred from one fiber to another (and not the optical signals) the adhesive bond coupler was successful. Additionally, an adhesive bond can be quickly performed for field applications. The signals from three locations across an aluminum plate were successfully monitored with a single FBG sensor. However, fabricating repeatable adhesive bond couplers with a fixed length was challenging. Therefore, Kim et al.

used a single drop of CA adhesive to minimize losses and make the couplers as consistent as possible [16], [39].

A stainless-steel mold-based design was used previously to fabricate CA acoustic couplers of a given length [54]. While this fabrication technique was successful in producing a coupler capable of transferring signal to the coupled fiber, the resulting coupler geometry was not ideal and therefore its performance was severely limited by losses through the coupler. While mold release was used, the small geometry of the mold resulted in partial removal of the coating when the coupler was demolded. Leading to an inconsistent outer diameter along the coupler length. In addition, the coupler edges were flat rather than tapered, resulting in a significant impedance mismatch at the waveguide-coupler interface, which caused partial signal reflections at these points. Likely contributing to the large return losses.

In this paper, a novel flow coating fabrication technique will be applied to the adhesively bonded coupler to improve the geometry of the as-fabricated coupler. Despite non-optimal acoustic properties CA was chosen primarily for the rapid gel time, workability, and low cost. By limiting the amount of CA deposited we also hope to enhance the signal transfer between the SMOF and minimize loss through the coupler. In addition, producing a better coupler geometry will allow the study of the coupler's length effect has on the coupling behavior and comparison to existing numerical models from the literature.

4.2 Experimental Methods

4.2.1 Coupler Fabrication

In this paper an acetone-based CA solution was used to fabricate CA couplers utilizing a flow coating process to limit the adhesive deposited on the surface of the two fibers. This method utilizes the capillary forces between two closely spaced cylinders to control the cross-sectional shape of the coupler during manufacturing. A schematic of the fabrication process can be seen in Figure 4.2. By dissolving the CA in a volatile solvent such as acetone, the surface tension of the mixture can be controlled to create a solution suitable for fabricating the coupler via flow coating. The coupler solution used in this experiment was comprised of 1.125 grams of Acetone mixed with roughly 0.125 grams of CA and a drop of blue water-based dye (~ 0.05 grams). The blue pigment was added to make the dimensions of the coupler more pronounced for measurement and identification under a microscope. The solution was mixed thoroughly before being applied. Producing a solution that was 9.6% CA by weight. When this solution is applied to closely spaced optical fibers a capillary bridge is formed. Only a small amount of solution within the capillary bridge membrane can resist gravitational forces, the excess solution falls into a runoff basin. Once the acetone has evaporated the CA is left deposited on the surface of the two fibers. The bridge helps control the shape of the final coupler and ensure that the majority of the adhesive is deposited between the fibers. Thus, minimizing the adhesive deposited and creating an acoustic coupler with a much smaller more uniform cross section.

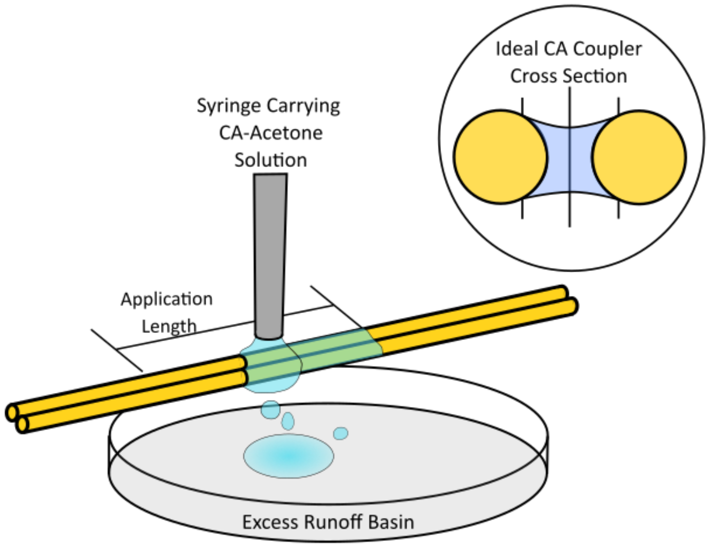

Figure 4.2 Schematic of the CA coupler flow-coating fabrication method.

The primary objective was to observe how couplers produced with the flow coating fabrication technique compared those fabricated by mold. The secondary objective was to observe coupler behavior as the length was reduced. Approximately 1 ml of CA solution was used to fabricate every coupler used in this experiment, however, to better accomplish each objective slight modifications to the fabrications process were implemented. In the first experiment the fiber alignment was maintained by hand as it would likely be performed in the field. Once the solution was applied, the CA was given roughly a minute to reach fixture strength before the fiber alignment was no longer maintained. Allowing the fibers to naturally rest for the remaining 12 hours to ensure a complete cure. Demonstrating the range of performance that can be expected with CA couplers fabricated with this method in field. A composite image of one of the couplers used in the first experiment can be seen in Figure 4.3(a). In this figure a checkerboard pattern can be seen in the background. This backdrop was created to aid in measuring the coupler. However, image stitching algorithms will scale, rotate and distort each image for proper blending. These techniques rendered the background inconsistent in final the composite image. For this reason, subsequent composite photos were taken without the checkered backdrop.

For the decreasing length experiment, two clamps were used to maintain fiber alignment over the entire course of the 12-hour period. This was done since the coupling coefficient is known to be heavily dependent on the spacing of the two waveguides. The clamps ensured that alignment and spacing between the fibers was uniform and consistent across the entire length of the coupler. An example of the alignment-controlled coupler can be seen in Figure 4.3(b).

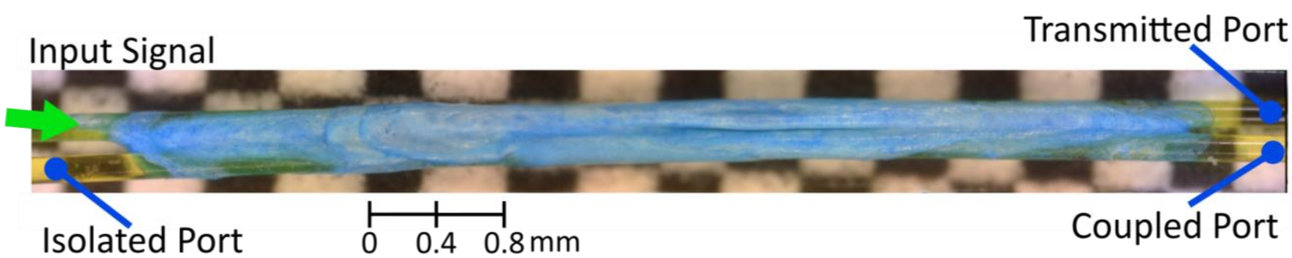

(a)

(b)

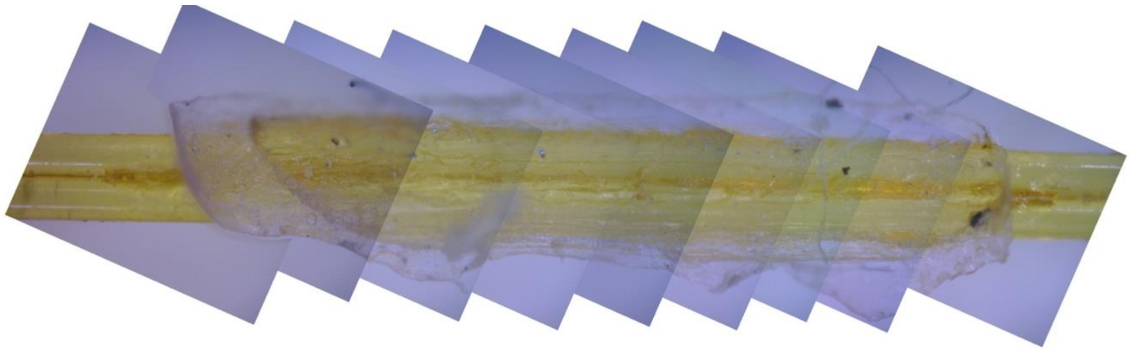

(c)

Figure 4.3 Composite Photo of: (a) 5.98 mm long coupler (coupler C) used in first experiment against checkered backdrop, (b) example of alignment-controlled coupler, and (c) 2.9 mm long molded coupler [54].

The core acoustic waveguide network consisted of two optical fibers. Both fibers used in this experiment were standard single mode optical fiber (SMF-28e) with a 15 µm thick polyimide coating. Couplers were applied to form a 2-by-2 coupler, the performance of each coupler was measured across 6 trials with the level of amplification applied to the PZT's excitation signal increased between each measurement. The length of each coupler was measured with calipers by utilizing the blue pigment to identify the coupled region. Once each coupler completed testing, they were removed from the optical fibers using pure acetone. Isopropyl alcohol was then used to prep the surface of the optical fibers before the new coupler was applied.

The purpose of the secondary objective is to discern the mechanism of signal transfer across the CA coupler. Should the performance be governed by coupled mode theory, the power distribution across the waveguide cores should vary with the coupler's length. Otherwise, the length of the coupler will only affect material losses caused by the presence of CA. To test this, coupler performance was repeatedly measured as the length of the coupler was steadily decreased. A small segment of the coupler's length was dissolved by touching a drop of pure acetone to the output end of the CA coupler. To ensure that the capillary forces would not inhibit adhesive removal, the optical fibers on the output side of the coupler were lightly spaced slightly. This process was simulated under a microscope in Figure 4.4 to demonstrate the reduction in length that is achievable.

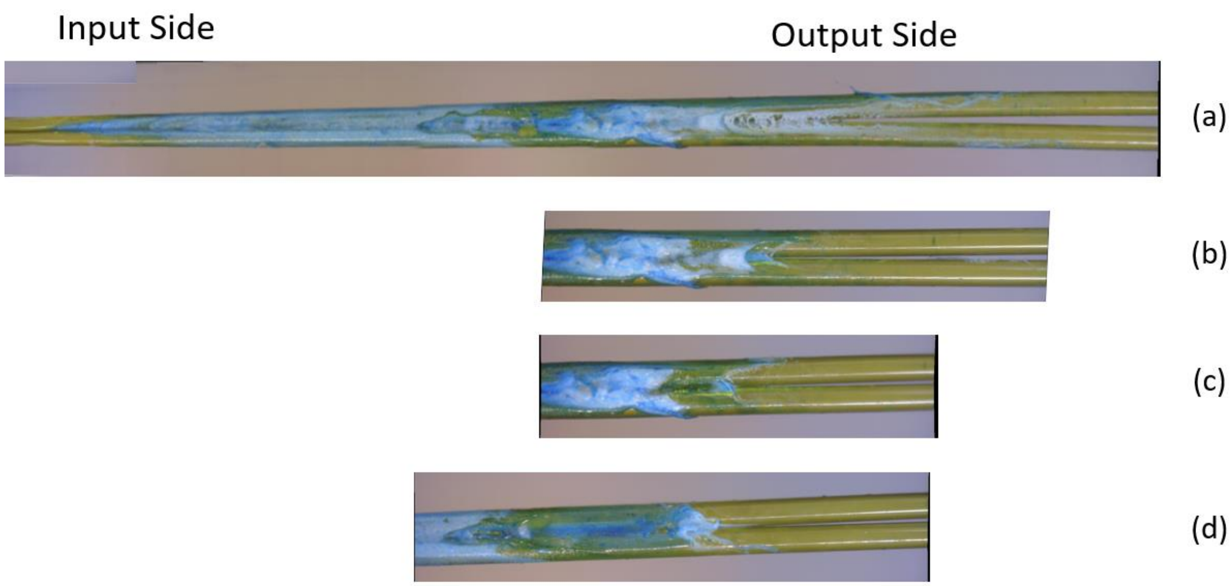

Figure 4.4 Aligned composite photo of: (a) flow coated acoustic coupler before length reduction, (b) after a single drop of acetone, (c) after a two drops of acetone, and (d) after a three drops of acetone.

4.2.2 Measurement of Coupler Performance

To measure the coupler performance, an acoustic wave was generated in one fiber and the amount of energy coupled in each direction measured, using the experimental arrangement shown in Figure 3. The first fiber was bonded to an aluminum plate embedded with a 2 cm x 1 cm centimeter thin CA film. This technique has been applied in the past to generate the L_{01} ultrasonic mode in an optical fiber [26], [55]. The other optical fiber was connected to the first fiber through the CA coupler. As a result, all acoustic measurements along this second fiber are a result of signal being transferred from the first fiber. The previously described acetone-CA solution was used to apply various couplers directly on the surface of the two fibers, creating a simple coupled fiber network. Four FBGs were located along all four ports of the 2-by-2 coupler so that the acoustic information entering and exiting the coupler was continuously monitored. This setup of the fiber network was chosen since it has been successfully used in the past to observe acoustic signal transfer between the two acoustic waveguides [41], [54].

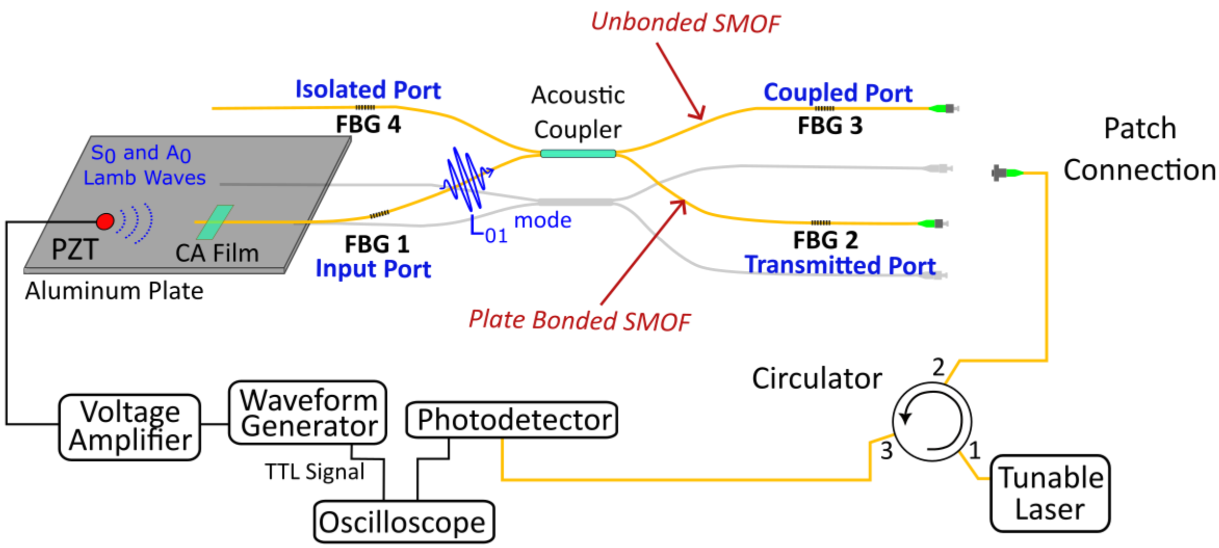

Figure 4.5 Experimental setup for measuring the performance of a 2-by-2 acoustic coupler.

A piezo-electric transducer (PZT) was excited to produce S_0 and A_0 Lamb waves in the aluminum plate 10 cm away from the CA thin film. After reaching the CA film, Lamb waves traveling along the structure would be confined to the SMOF as the L_{01} extensional mode. A 609.6 mm x 609.6 mm and 0.8 mm thick 6061 aluminum plate was used in these experiments. The edges of the plate were covered with 7.5 cm wide strips of an elastomeric damping material (Dynamat®) on both sides to damp signals and prevent signal reflection at the plate edges.

Which prevented any secondary signals from entering the fiber network. The PZT was placed roughly 12 cm from the center edge of one of the Dynamat boundaries. Leaving the CA film 24 cm from the opposite Dynamat boundary. An arbitrary waveform generator (AWG) and amplifier were used to actuate the PZT. The AWG was set to produce a 5.5 cycle 300 kHz Hanning window function, repeating this waveform every 10 milliseconds. The TTL trigger signal from the AWG was used to synchronize the oscilloscope's measurements with each PZT excitation.

To remove noise that was not periodically repeated within the measurement window the oscilloscope was set to average across 4,096 cycles of PZT excitation. A high-speed photodetector (PD) converted the optical intensity returned by a FBG into a voltage, which was then interpreted by the oscilloscope. The signal was measured at a sample rate of 5 GHz for the 400 us that followed PZT excitation. This process was repeated for each of the four FBG used in the experiment. The FBGs within each fiber were interrogated by either adjusting the wavelength of the tunable laser or manually switching the connection to the circulator. So before recording any measurement, the reflected spectrum of each FBG was measured to calibrate the strain reading.

4.3 Results

4.3.1 Performance of Flow Coated Couplers

The performance of the flow coated coupler was calculated from the FBG measurements for each experiment. The coupler performance and losses were then compared to previously fabricated CA couplers.

For a propagating acoustic mode, the energy is stored as a strain energy across the waveguides cross section. Each FBG measures the strain along the core of the fiber at a fixed location in the fiber network across time. With the thin rod assumption, the strain across the cross section can be assumed to be uniform. While the total energy at a fixed point is proportional to amplitude of the displacement squared [56]. Thus, for discreet time signals the strain energy, E, that passes through a fixed location is equal to

$$E = \ const \cdot \sum_{t = \ t_s}^{t_e - 1} |X(t)|^2 \tag{4.1}$$

Where X, corresponds to the entire series of strain measurements recorded by the FBG, and t_s and t_e correlate to start and end times energy is calculated across [38]. The constant term is dependent on the mass density of the optical fiber and the cross-sectional contribution to the total energy. Equation 4.1 was used to calculate the energy of the waveforms measured by each FBG immediately following the signal coupler interaction. As well as the energy of the incident signal that entered the coupler from the Input (FBG 1) port. By normalizing the results with the incident waveform energy, the constant term cancels and the energy received by each FBG is expressed as a proportion of the incident signal.

It is important to note that so long as the length of the time interval [t_s, t_e] is consistent across all energy calculations, the relative difference in energy between two signals will be equivalent to a relative difference in power. In this experiment it took 39 μs for the entire incident waveform to pass FBG 1. Since the longitudinal mode of a single mode optical fiber is nondispersive up to 10 to 15 MHz, the group velocity can be assumed constant for all frequencies within the wave packet [33]. Allowing the 39 μs long time interval to be used for the remaining energy calculations. Furthermore, the exact location the coupler was applied in the fiber network was not perfectly consistent between each of the fabricated couplers. So, a cross correlation was used to identify the optimal values of t_s and t_e for each FBG's energy calculation.

For every coupler tested this procedure was repeated for the 6 separate PZT excitation magnitudes. The results of the 6 trials were then averaged for each of the flow coated couplers made and the results tabulated in Table 4.1 below.

Table 4.1 Measured power ratios for coupler ports. Molded coupler data from [54].

		Power (% P_{out}/P_{in})			
Coupler Name	Length *(mm)*	FBG 1 Input r_1	FBG 2 Transmitted r_2	FBG 3 Coupled r_3	FBG 4 Isolated r_4
A	4.2	22.9	19.9	14.0	4.03
B	5.16	14.0	13.7	16.2	14.9
C	5.98	3.04	14.7	12.6	0.45
D	6.65	8.16	25.5	26.4	8.07
E	7.15	23.3	26.9	23.7	14.1
F	8.85	21.8	19.6	12.5	9.84
G	9.28	17.7	19.8	16.8	19.4
H	10.81	11.1	29.1	19.1	3.63
Molded coupler	2.9	11.3	13.0	4.33	0.525

It's clear that the signal transference capabilities displayed by the flow coated coupler was superior to the coupler fabricated via stainless-steel mold. Across the board the percentage of signal power received by each port of the 2-by-2 coupler increased with the new fabrication method. Demonstrating that the material losses to the coupler decreased when the CA applied to the fibers was reduced. When one considers that signal attenuation along a waveguide is expressed per unit length the reduction in attenuation becomes even more apparent. As every coupler tested was significantly longer than the molded coupler.

With the mold fabricated coupler, only about 5 percent of the initial signal was transferred to the opposite fiber and overall, 70 percent of the signal power was lost through the coupler. While the flow coated couplers consistently transferred about 20 to 30 percent of the signal power to the opposite fiber. Losing only 12 to 40 percent of the signal power through the coupler. One notable outlier is coupler C, which lost 69 percent of signal power through the coupler. However, even in this case the signal transfer to the opposite fiber was almost three times larger than the molded coupler. Showing a drastic increase in signal transference and signal preservation was achieved with a simple modification to the fabrication method.

Despite being nearly twice the length of the 4.2 mm coupler, the 7.15 mm coupler displayed the lowest levels of signal loss. Signifying that signal attenuation per unit length was not uniform between the various couplers. This could point to inconsistent CA deposition between the different flow coated couplers fabricated for this experiment. Another factor to consider is the observed tapering that occurred as a result of the flow coating fabrication method. Unlike the molded coupler, the boundary between the optical fiber and the flow coated coupler was tapered. The different levels of tapering are best observed in Figure 4.3. The tapering likely assisted impedance matching in some cases, particularly in couplers C, D and H. In all three cases the signal strength reflected and sent to the isolated port (FBG 1 and FBG 4) was small relative to the signal sent to the coupled and transmitted ports (FBG 3 and FBG 2). However, the use of capillary forces for adhesive distribution meant that the spacing of the fibers heavily influenced the length and shape of the tapered region in the final coupler. More separation between the optical fibers will result in a more pronounced taper. Therefore, the effects of tapering are much less pronounced in the alignment-controlled couplers discussed in the next section.

Our expectations on how changing the fabrication method would affect the coupler performance overall align with the results. However, the results do not support the previous conclusion that an impedance mismatch between the coupler and SMOF was the dominant factor responsible for input reflections at the SMOF-coupler interface. We expected that the flow coated fabrication technique would reduce the cross section of the coupler and reduce the impedance mismatch, thereby also reducing the partial reflection measured at the input port (FBG 1). In addition, the tapered boundaries that were observed are typically included in waveguide designs to assist in impedance matching. However, the amount of signal reflected was very inconsistent across the flow coated couplers and, in some cases, exceeded the molded coupler. If one were to consider the parameters that govern the characteristic acoustic impedance of a waveguide [50]:

$$Z = \frac{\rho v}{S} \tag{4.2}$$

Where, ρ is the effective density, v is the speed of sound in the waveguide and S is the cross-sectional area. One could deduce that adding more CA on the surface of the optical fibers could only increase the impedance mismatch. So, for an ideal adhesive coupler where the presence of CA is effectively ignored. The coupled region would consist of just the two optical fibers, doubling the effective cross section. Which would correspond to an 11.1 percent reflection of incident signal power in this idealized case. Despite the lower density, slower wave velocity, lack of taper, and larger cross section the molded coupler displayed reflections of this magnitude. Indicating there is another factor contributing to return losses. A possible explanation for this is the CA coupler behaves as a resonator causing some form of resonant scattering. Where localized resonant modes of the coupler are excited by the propagating wave which cause constructive or destructive interference [57]. Leading to frequency dependent reflection and transmission at the boundary of a waveguide discontinuity [58], [59]. One form of resonant scattering, Fano resonance, has been recently demonstrated in an elastic waveguide with a similar geometric change along its axis by Kato et al. [60]. To test if resonant scattering occurs in this application, future work should apply CA to the surface of a single optical fiber measuring reflectance and transmittance across signal frequency. If present, the shape of the resulting frequency transmittance curve can be used to identify the type of resonant scattering.

4.3.2 Decreasing Coupler Length Experiment

In this experiment the signal power directed to the four ports of the alignment-controlled coupler was measured as the length of the coupler was steadily reduced. By carefully applying pure acetone along the output end of the coupler small segments of the coupler were removed between each measurement. The relative power exiting each port of the coupler was calculated using the method described in the previous section. The first coupler tested in this experiment began at a length of 12.08 mm and its length was reduced 25 times until 3.94 mm of the coupler remained. To observe the effect of length across a smaller span, the process was again repeated for a 12.47 mm long coupler that was reduced a total of 12 times until 9.67 mm of the coupler remained. The percentage of incident power received at each port following the signal-coupler interaction can be seen in Figure 4.6 below.

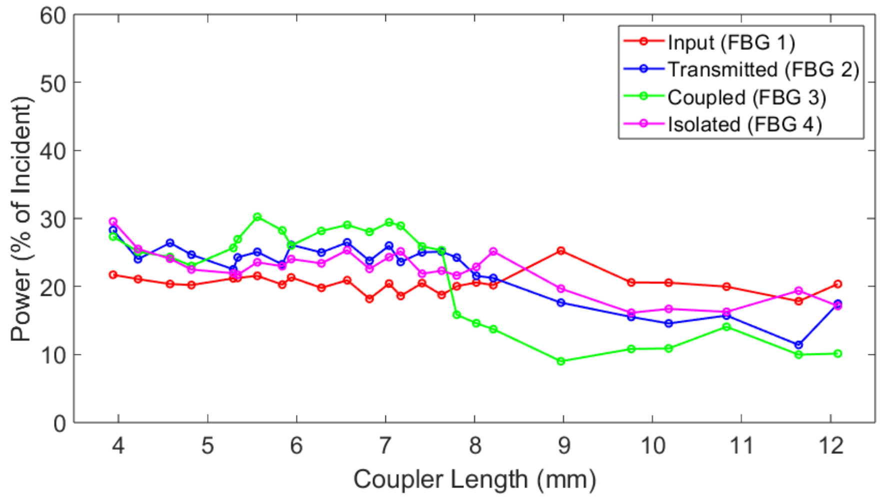

(a)

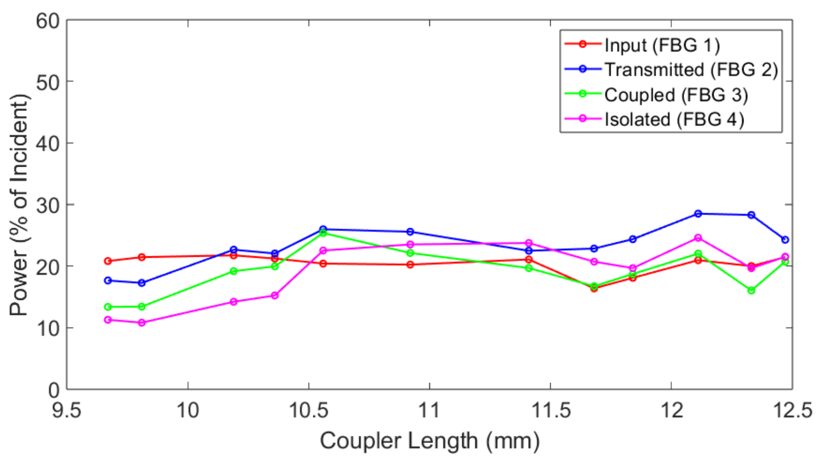

(b)

Figure 4.6 The relative power received by each port of the coupler as length was decreased for the (a) 1st long span coupler and (b) the 2nd short span coupler.

When the signal entered the coupler, a partial reflection of the initial signal was observed returning to FBG 1, called return loss. Figure 4.6 illustrates that the percentage of return losses (FBG 1) was roughly constant across all lengths tested. Hence, coupler's length had no bearing on the magnitude of input reflections. The average return loss was close to equal for both the long and short span couplers. Considering the alignment and contact between the optical fibers was strictly maintained for both couplers. The cross-sections of both couplers will be close to equal and the tapering at the boundaries minimal. Supporting conclusion made in the previous section that both cross section and tapering at the boundary influence the input reflections.

The sum of power that exited all four ports of the coupler was used to determine the overall loss through the coupled region, seen in Figure 4.7. For the 1st long span coupler the overall signal losses decreased with the coupler's length as expected. Once the length of the coupler decreased below ~ 8 mm the overall magnitude of signal loss became indistinguishable from measurement noise from the oscilloscope averaging operation. Resulting in instances with more than 100% of incident signal power accounted for across the four ports. However, in such cases the excess energy reported was marginal. Demonstrating that flow coated CA couplers are more optimized to minimize signal loss. Excelling in an area of performance that is considered the main limitation with the CA couplers tested previously. For the 2nd coupler, it began the experiment at a length where losses were already minimal, with a noticeable spike in loss in the two shortest lengths. In Figure 5(b), this spike is seen as reduction in power delivered to the coupled, isolated, and transmitted ports (FBG 3, FBG 4, and FBG 2). The cause for the increase in signal loss is currently not known for certain. However, a defect or debris may have been introduced to the coupler, since the return loss was the only parameter to be unaffected.

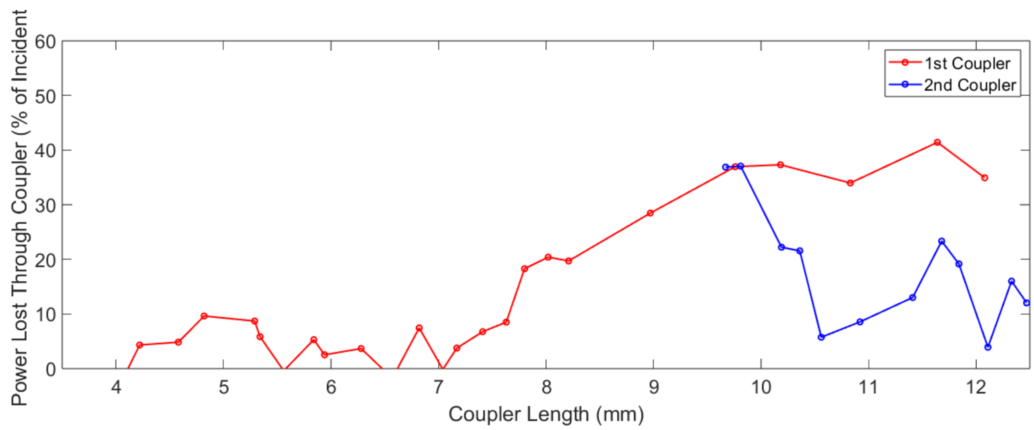

Figure 4.7 The overall signal loss for the 1st long span and 2nd short span couplers.

Coupling ratio, coupling factor and the isolation are typical performance specifications of a directional coupler. The coupling ratio and factor define the power splitting and signal transference through the coupler respectively. While isolation is defined by signal sent between adjacent ports, in this case the input and isolated ports (FBG 1 and FBG 4). These quantities are defined by the following equations.

$$Coupling\ Ratio(dB) = 10\ \log\left(\frac{r_2 + r_3}{r_3}\right) \tag{4.3}$$

$$Coupling\ Factor\ (dB) = 10\ \log(r_3) \tag{4.4}$$

$$Isolation\ (dB) = -10\ \log(r_4) \tag{4.5}$$

Where, r_n is the ratio of initial power received by one of the four ports of the coupler, and n designates which port in accordance with the FBG numbering. The performance of both couplers across all lengths can be seen in Figure 4.8. For the long span coupler, the isolation generally decreased with length Figure 4.8(b). Once isolation was reduced to 6 dB the length no longer had any influence on isolation. For the short span coupler, the isolation began at this 6 dB limit and only increased when the defect was thought to be introduced, Figure 4.8(d). The same trends were observed along the coupling ratio and coupling factor curves in Figure 4.8. Where there was a threshold level of performance, that when once met, meant that length no longer had any meaningful effect on performance. The coupling ratio never receded below 3dB in both tests, corresponding to a 50/50 power split across the coupled and transmitted ports (FBG 3 and FBG 2). The maximum coupling factor observed was limited to -5.5 and -6 dB for the long span and short span couplers respectively. At these points the performance correlates with an even power distribution across the isolated, coupled, and transmitted ports (FBG 4, FBG 3, and FBG 2). Such behavior is not characteristic of coupled mode theory.

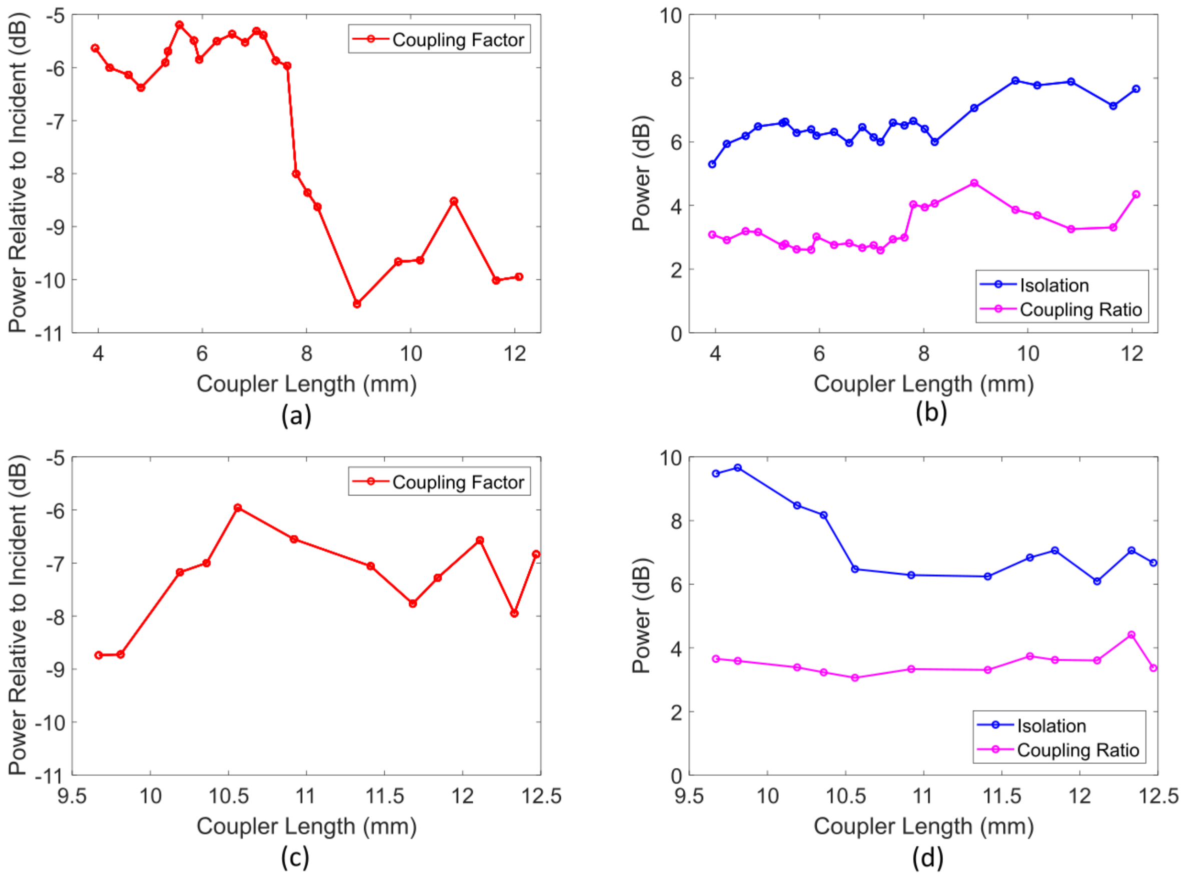

Figure 4.8 Plot of directional coupler performance across length showing; (a) the coupling factor and (b) isolation and coupling ratio of the 1st long span coupler, and (c) the coupling factor and (d) isolation and coupling ratio of the 2nd short span coupler.

When the losses through the couplers were minimal, they demonstrated a tendency to reflect a fixed amount of energy at the SMOF-coupler interface. With an average of 21 percent of the incident signal power reflected. The remaining acoustic energy was then split evenly between the other three ports of the coupler. Roughly 25 percent of incident signal power was then sent to the remaining three ports.

Kim et al. previously performed FEA simulations on the signal coupling between two optical fibers that shared a CA coating layer [27]. It is from this simulation we expected a weakly periodic relationship between power sent to the output ports and coupler length. With fluctuations slowly diminishing until a steady state energy distribution between the fibers is reached. The second coupler tested for this experiment was specifically chosen because the simulation predicted that periodic behavior occurs across 2 mm of the coupler's length. However, there were no discernible fluctuations in the performance exhibited across either coupler.

One possible explanation for this difference is the damping introduced by the CA. In the simulation, the periodic behavior vanished as the Rayleigh damping coefficient of the adhesive layer was increased. Indicating that the signal transfer via evanescence diminishes with lossy coupler materials. It is likely that the periodic relationship between coupler length and the direction of signal coupling is more prevalent when: 1) there is sufficient mode confinement to the waveguide core and 2) stiff non-lossy acoustic materials are used for the coupler. While the second point can be realistically addressed by including additives to adjust the properties of the CA as needed. Better mode confinement is only possible by using a larger diameter core for the waveguide, which would inhibit leakage of the L_{01} mode into the surrounding adhesive [36]. In this case it would require the use of thicker silica rods.

4.4 Conclusion

To conclude the flow coating manufacturing method for fabricating CA acoustic couplers was successfully implemented. The objective of reducing the signal loss through the coupler was successfully achieved. The experiments performed in this paper demonstrated the superiority of this fabrication technique to mold based or freehanded methods. On average the relative signal transfer to the opposite fiber increased by a factor of 5.6 when compared to the molded coupled.

The results demonstrate that the signal transfer through previously studied couplers was heavily limited by material losses to the CA. The flow coating technique limited the CA deposited on the surface of the optical fibers, and as a result, the losses observed through the coupler were minimal. Even demonstrating that losses through the coupler are negligible with sufficiently short coupler lengths. Unexpectedly, the molded coupler displayed lower return losses despite the larger impedance mismatch. Showing that another factor influenced input reflections aside from the cross section of the coupler and taper at the boundary.

The results also unexpectedly showed that at short lengths, power exiting the coupler was evenly split across the coupled, transmitted, and isolated ports. This behavior was observed independent of the length of the coupler. While this behavior should be further studied, the main objective of this work was successfully achieved. As flow coated CA couplers are not nearly as limited by the material losses and have demonstrated better suitability for sensing applications.

4.5 Acknowledgements

The authors thank the Office of Naval Research (ONR) (N00014-20-1-2583) for support of this research.

CHAPTER 5

Conclusion and Recommendations for Future Work

This dissertation demonstrates that the sensing capabilities of coupled fiber network can be enhanced with several simple yet effective changes. The first change involves increasing the diameter of the transmission fibers that are responsible for guiding the acoustic signal to the FBG. Exchanging a polyimide coated 125 µm optical fiber for a 400 µm uncoated silica fiber will reduce the attenuation along the transmission fiber by a factor of 6. The larger diameter fiber will be less susceptible to signal leakage into the environment and provide better mode confinement. In addition, if good contact between the waveguides is maintained, the larger diameter will be capable of transferring more acoustic power to the sensing fiber [41].

The second change involves utilizing the flow coating fabrication method. The experiment demonstrated both signal preservation and transference were enhanced through this fabrication technique. As less CA is deposited on the surface of the fibers the material losses to the adhesive are diminished. The capillary forces ensure that the bulk of the CA deposited is in between the fibers resulting in excellent contact between the fibers despite the small amount of adhesive. To further enhance the performance, research into incorporating ceramic additives in the CA-acetone solution may help control the acoustic properties and lower losses through the coupler. A comprehensive study on tapering at the coupler boundary and how to control the taper during fabrication will help further minimize return losses.

Almost all previously studied CA couplers, including the couplers presented in this work, are constructed in a parallel waveguide configuration. For electromagnetic couplers constructed in this configuration they are called coupled line directional couplers. In this configuration signal transference is the result of evanescent field interaction in a shared cladding region. The behavior of such interaction is described by coupled mode theory and predicts power splitting at the output will periodically fluctuate with coupler length. Unfortunately, such a relationship was not observed in the CA couplers measured in these experiments. The results suggest that the L_{01} mode is not strictly confined to the optical fiber and will be distributed across the entire cross-section of the coupled region. Preventing the longitudinal mode from interacting with the CA as it would a cladding layer.

However, throughout every experiment the presence of CA was observed to cause an impedance change along the optical fiber. There is potential to utilize this effect to create a coupling device in a different configuration. A quadrature hybrid or branch-line coupler is a type of directional coupler configuration that uses secondary lines that directly connect the waveguides together [61]. The layout of the secondary lines in a quadrature hybrid coupler is seen in Figure 5.1. In this configuration the behavior of the coupler is determined by the impedance along four secondary lines that form the coupler. Given how easily CA can be used to adjust the impedance along the optical fiber, a branch line configuration may be a more viable coupler design that would allow for controllable parameters. In this regard my recommendation for future work is to perform an FEA simulation of single mode optical fibers that are embedded in CA film that forms a quadrature hybrid coupler shape.

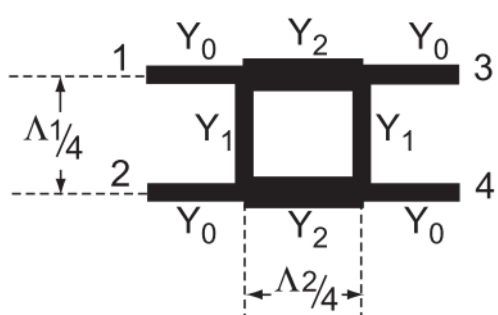

Figure 5.1 Quadrature Hybrid coupler with impedances of each line *Y* [47].

REFERENCES

[1] N. K. Mutlib, S. Bin Baharom, A. El-Shafie, and M. Z. Nuawi, “Ultrasonic health monitoring in structural engineering: buildings and bridges,” 2015, doi: 10.1002/stc.1800.

[2] W.J. Staszewski, C. Boller, and G.R. Tomlinson, *Health Monitoring of Aerospace Structures*. Wiley, 2003. doi: 10.1002/0470092866.

[3] C. Zhou *et al.*, “Probability-based diagnostic imaging using hybrid features extracted from ultrasonic Lamb wave signals,” *Smart Mater Struct*, vol. 20, no. 12, p. 125005, Nov. 2011, doi: 10.1088/0964-1726/20/12/125005.

[4] J. B. Ihn and F. K. Chang, “Pitch-catch Active Sensing Methods in Structural Health Monitoring for Aircraft Structures,” *http://dx.doi.org.prox.lib.ncsu.edu/10.1177/1475921707081979*, vol. 7, no. 1, pp. 5–19, Mar. 2008, doi: 10.1177/1475921707081979.

[5] D. N. Alleyne and P. Cawley, “The Interaction of Lamb Waves with Defects,” *IEEE Trans Ultrason Ferroelectr Freq Control*, vol. 39, no. 3, pp. 381–397, 1992, doi: 10.1109/58.143172.

[6] A. Ghadami, M. Behzad, · Hamid, and R. Mirdamadi, “Damage identification in multi-step waveguides using Lamb waves and scattering coefficients,” *Archive of Applied Mechanics*, vol. 88, pp. 1009–1026, 2018, doi: 10.1007/s00419-018-1355-0.

[7] Z. Nazarchuk, V. Skalskyi, and O. Serhiyenko, “Propagation of elastic waves in solids,” *Foundations in Engineering Mechanics*, no. 9783319493480, pp. 29–73, 2017, doi: 10.1007/978-3-319-49350-3_2/TABLES/5.

[8] D. H. Kim, Y. H. Kim, and C. G. Kim, "Directivity evaluation of fiber optic sensor for detecting Lamb waves," *Smart Mater Struct*, vol. 14, no. 5, p. 1037, Sep. 2005, doi: 10.1088/0964-1726/14/5/042.

[9] I. M. Perez, H. Cui, and E. Udd, "Acoustic emission detection using fiber Bragg gratings," *https://doi-org.prox.lib.ncsu.edu/10.1117/12.435542*, vol. 4328, pp. 209–215, Aug. 2001, doi: 10.1117/12.435542.

[10] Z. Su and L. Ye, "Sensors and Sensor Networks," in *Identification of Damage Using Lamb Waves*, vol. 48, Springer, London, 2009, pp. 99–142. doi: 10.1007/978-1-84882-784-4_4/COVER.

[11] B. Culshaw, G. Thursby, D. Betz, and B. Sorazu, "The Detection of Ultrasound Using Fiber-Optic Sensors," *IEEE Sens J*, vol. 8, no. 7, 2008, doi: 10.1109/JSEN.2008.927240.

[12] D. C. Betz *et al.*, "Acousto-ultrasonic sensing using fiber Bragg gratings," *Smart Mater Struct*, vol. 12, no. 1, p. 122, Jan. 2003, doi: 10.1088/0964-1726/12/1/314.

[13] G. R. Kirikera, O. Balogun, and S. Krishnaswamy, "Adaptive Fiber Bragg Grating Sensor Network for Structural Health Monitoring: Applications to Impact Monitoring," *http://dx.doi.org/10.1177/1475921710365437*, vol. 10, no. 1, pp. 5–16, Apr. 2010, doi: 10.1177/1475921710365437.

[14] J. Frieden, J. Cugnoni, J. Botsis, and T. Gmür, "Low energy impact damage monitoring of composites using dynamic strain signals from FBG sensors – Part I: Impact detection and localization," *Compos Struct*, vol. 94, no. 2, pp. 438–445, Jan. 2012, doi: 10.1016/J.COMPSTRUCT.2011.08.003.

[15] H. Tsuda and J.-R. Lee, “Fiber optic liquid leak detection technique with an ultrasonic actuator and a fiber Bragg grating,” *Optics Letters, Vol. 30, Issue 24, pp. 3293-3295*, vol. 30, no. 24, pp. 3293–3295, Dec. 2005, doi: 10.1364/OL.30.003293.

[16] J. M. Kim, J. Wee, and K. Peters, “Demonstration of Coherent Interference between Acoustic Waves Using a Fiber Ring Resonator,” *Sensors (Basel)*, vol. 22, no. 11, Jun. 2022, doi: 10.3390/S22114163.

[17] R. Soman, J. Wee, and K. Peters, “Optical Fiber Sensors for Ultrasonic Structural Health Monitoring: A Review,” 2021, doi: 10.3390/s21217345.

[18] G. Coppola *et al.*, “Analysis of feasibility on the use of fiber Bragg grating sensors as ultrasound detectors,” *https://doi-org.prox.lib.ncsu.edu/10.1117/12.435523*, vol. 4328, pp. 224–232, Aug. 2001, doi: 10.1117/12.435523.

[19] A. Minardo, A. Cusano, R. Bernini, L. Zeni, and M. Giordano, “Response of fiber bragg gratings to longitudinal ultrasonic waves,” *IEEE Trans Ultrason Ferroelectr Freq Control*, vol. 52, no. 2, pp. 304–312, Feb. 2005, doi: 10.1109/TUFFC.2005.1406556.

[20] Z. Li, L. Pei, B. Dong, C. Ma, and A. Wang, “Analysis of ultrasonic frequency response of surface attached fiber Bragg grating,” *Applied Optics, Vol. 51, Issue 20, pp. 4709-4714*, vol. 51, no. 20, pp. 4709–4714, Jul. 2012, doi: 10.1364/AO.51.004709.

[21] R. P. Depaula, L. Flax, J. H. Cole, and J. A. Bucaro, “Single-Mode Fiber Ultrasonic Sensor,” *IEEE J Quantum Electron*, vol. 18, no. 4, 1982.

[22] C. B. Yun and J. Min, “Smart sensing, monitoring, and damage detection for civil infrastructures,” *KSCE Journal of Civil Engineering*, vol. 15, no. 1, pp. 1–14, Aug. 2011, doi: 10.1007/S12205-011-0001-Y/METRICS.

[23] F. Zhang *et al.*, “Dynamic fiber Bragg grating sensor array with increased wavelength-division multiplexing density and low crosstalk,” *https://doi-org.prox.lib.ncsu.edu/10.1117/1.OE.56.3.037101*, vol. 56, no. 3, p. 037101, Mar. 2017, doi: 10.1117/1.OE.56.3.037101.

[24] Z. Luo, H. Wen, H. Guo, and M. Yang, “A time-and wavelength-division multiplexing sensor network with ultra-weak fiber Bragg gratings,” 2013, doi: 10.1364/OE.21.022799.

[25] S. Jinachandran and G. Rajan, “Fibre Bragg Grating Based Acoustic Emission Measurement System for Structural Health Monitoring Applications,” 2021, doi: 10.3390/ma14040897.

[26] J. Wee, P. Bradford, B. Wells, K. Peters, and D. Hackney, “Increasing signal amplitude in fiber Bragg grating detection of Lamb waves using remote bonding,” *Applied Optics, Vol. 55, Issue 21, pp. 5564-5569*, vol. 55, no. 21, pp. 5564–5569, Jul. 2016, doi: 10.1364/AO.55.005564.

[27] J. Kim, “Characterization of Acoustic Wave Coupling between Cylindrical Waveguides for Sensing Applications,” North Carolina State University, Raleigh, 2022.

[28] J. Tschepe, K. Desinger, J. Helfmann, M. Herrig, and G. Miiller, “The Transmission of High and Low Power Acoustical Transient Waves Via Optical Fibers.”

[29] W. A. Leal, | Mateus, B. R. Carneiro, T. A. M. G. Freitas, and R. M. Ribeiro, “Low-frequency detection of acoustic signals using fiber as an ultrasonic guide with a distant in-fiber Bragg grating”, doi: 10.1002/mop.31061.

[30] J. Wee, D. Hackney, and K. Peters, “Preferential directional coupling to ultrasonic sensor using adhesive tape,” *https://doi-org.prox.lib.ncsu.edu/10.1117/1.OE.58.7.072003*, vol. 58, no. 7, p. 072003, Jan. 2019, doi: 10.1117/1.OE.58.7.072003.

[31] Y. Jiang, J. Yue, J. Gao, al -, J.-R. Lee, and H. Tsuda, “Sensor application of fibre ultrasonic waveguide,” *Meas Sci Technol*, vol. 17, no. 4, p. 645, Feb. 2006, doi: 10.1088/0957-0233/17/4/006.

[32] B. M. Beadle and R. S. Weis, “Longitudinal Vibrations of a Silica Fiber Segment Characterized Using a Fiber Bragg Grating,” 1998.

[33] J. R. Lee and H. Tsuda, “Investigation of a fibre wave piezoelectric transducer,” *Meas Sci Technol*, vol. 17, no. 9, p. 2414, Aug. 2006, doi: 10.1088/0957-0233/17/9/007.

[34] R. N. Thurston, “Elastic waves in rods and clad rods,” *J Acoust Soc Am*, vol. 64, no. 1, pp. 1–37, Jul. 1978, doi: 10.1121/1.381962.

[35] C. Jen, “Leaky Modes in Weakly Guiding Fiber Acoustic Waveguides,” 1986.

[36] A. Safaai-Jazi, C. K. Jen, G. W. Farnell, and J. F. Bussiere, “LONGITUDINAL MODES IN WEAKLY GUIDING FIBER ACOUSTIC WAVEGUIDES.,” *Ultrasonics Symposium Proceedings*, pp. 1134–1138, 1985, doi: 10.1109/ULTSYM.1985.198694.

[37] A. Safaai-Jazi, “ANALYSIS AND DESIGN OF ACOUSTIC FIBER COUPLER.,” *Ultrasonics Symposium Proceedings*, pp. 433–437, 1987, doi: 10.1109/ULTSYM.1987.198997.

[38] C. Schaal, S. Bischoff, and L. Gaul, “Energy-based models for guided ultrasonic wave propagation in multi-wire cables,” *Int J Solids Struct*, vol. 64–65, pp. 22–29, Jul. 2015, doi: 10.1016/J.IJSOLSTR.2015.03.010.

[39] J. M. Kim, S. Aboubakr, and K. Peters, “Extension of Fiber Bragg Grating Ultrasound Sensor Network by Adhesive Couplers,” *Photonics*, vol. 10, no. 12, Dec. 2023, doi: 10.3390/PHOTONICS10121366.

[40] A. L. Matthews, K. A. Murphy, R. E. Rogers, and R. O. Claus, "ACOUSTIC FIBER WAVEGUIDE COUPLER.," *Ultrasonics Symposium Proceedings*, pp. 629–631, 1987, doi: 10.1109/ULTSYM.1987.199034.

[41] J. M. Kim, J. Wee, C. Marashi, and K. Peters, "Acoustic wave coupling between optical fibers of different geometries," *Applied Optics, Vol. 60, Issue 36, pp. 11042-11049*, vol. 60, no. 36, pp. 11042–11049, Dec. 2021, doi: 10.1364/AO.441494.

[42] G. Wild and S. Hinckley, "Acousto-Ultrasonic Optical Fiber Sensors: Overview and State-of-the-Art," *IEEE Sens J*, vol. 8, no. 7, 2008, doi: 10.1109/JSEN.2008.926894.

[43] H. Tsuda, "Ultrasound and damage detection in CFRP using fiber Bragg grating sensors," 2005, doi: 10.1016/j.compscitech.2005.07.043.

[44] B. Lissak, A. Arie, and M. Tur, "Highly sensitive dynamic strain measurements by locking lasers to fiber Bragg gratings," 1998.

[45] L.-B. Yang, L.-F. Hu, Q. Wu, and Y. Okabe, "Investigation of an integrated fiber laser sensor system in ultrasonic structural health monitoring," 2016, doi: 10.1088/0964-1726/25/3/035020.

[46] Q. Wu and Y. Okabe, "High-sensitivity ultrasonic phase-shifted fiber Bragg grating balanced sensing system," 2012, Accessed: Jan. 10, 2024. [Online]. Available: http://assets.newport.com/webDocuments-EN/images/15192.pdf

[47] Leo G. Maloratsky, *RF and Microwave Integrated Circuits Passive Components and Control Devices*. Burlington: Newnes, 2004.

[48] E. Drescher-Krasicka and J. A. Simmons, "Leaky axisymmetric modes in infinite clad rods. II Leaky axisymmetric modes in infinite clad rods. II," *J. Acoust. Soc. Am*, vol. 92, pp. 1091–1105, 1992, doi: 10.1121/1.404037.

[49] C.-K. Jen, A. Safaai-Jazi, and G. W. Farnell, “Leaky modes in weakly guiding fiber acoustic waveguides,” *IEEE Trans Ultrason Ferroelectr Freq Control*, vol. 33, no. 6, pp. 634–643, 1986, doi: 10.1109/T-UFFC.1986.26878.

[50] W. M. Robertson, I. Shirk, and E. Campbell, “Acoustic waveguide impedance matching via Helmholtz resonator mediated extraordinary acoustic transmission,” *AIP Adv*, vol. 9, no. 3, p. 35013, Mar. 2019, doi: 10.1063/1.5083906/1032363.

[51] P. Regtien and E. Dertien, “Acoustic sensors,” *Sensors for Mechatronics*, pp. 267–303, Jan. 2018, doi: 10.1016/B978-0-12-813810-6.00009-4.

[52] R. Yasir *et al.*, “Measurement Science and Technology Ultrasonic frequency response of fiber Bragg grating under direct and remote adhesive bonding configurations,” *Measurement Science and Technology Meas. Sci. Technol*, vol. 33, p. 6, 2022, doi: 10.1088/1361-6501/ac2fea.

[53] L. Han, M. Wang, L. Chai, D. Liu, W. Zhang, and W. Zhang, “Damage Monitoring and Localization Imaging of Aluminum Alloy Thin-Walled Structure Based on Remote Bonding Fiber Bragg Gratings Sensing,” *Materials*, vol. 17, no. 3, Feb. 2024, doi: 10.3390/MA17030652.

[54] C. Marashi and K. Peters, “Performance and Stability Analysis of Cyanoacrylate Acoustic Coupler for Sensing Applications ,” *In preparation*, 2023.

[55] C. Davis, C. Rosalie, P. Norman, N. Rajic, J. Habel, and M. Bernier, “Remote Sensing of Lamb Waves Using Optical Fibres - An Investigation of Modal Composition,” *Journal of Lightwave Technology*, vol. 36, no. 14, pp. 2820–2826, Jul. 2018, doi: 10.1109/JLT.2018.2816563.

[56] S. K. Lee, B. R. Mace, and M. J. Brennan, “Wave propagation, reflection and transmission in non-uniform one-dimensional waveguides,” *J Sound Vib*, vol. 304, no. 1–2, pp. 31–49, Jul. 2007, doi: 10.1016/J.JSV.2007.01.039.

[57] A. E. Miroshnichenko, S. Flach, and Y. S. Kivshar, “Fano resonances in nanoscale structures,” *Rev Mod Phys*, vol. 82, no. 3, pp. 2257–2298, Aug. 2010, doi: 10.1103/REVMODPHYS.82.2257/FIGURES/43/MEDIUM.

[58] L. Xiong, W. Bi, Y. Aurégan, and Y. Aur, “Fano resonance scatterings in waveguides with impedance boundary conditions,” *J Acoust Soc Am*, vol. 139, no. 2, pp. 764–772, Feb. 2016, doi: 10.1121/1.4941568.

[59] S. Hein, W. Koch, and L. Nannen, “Trapped modes and Fano resonances in two-dimensional acoustical duct-cavity systems,” *J. Fluid Mech*, vol. 692, p. 257, 2012, doi: 10.1017/jfm.2011.509.

[60] H. Kato and H. Kato, “Fano resonance of an elastic waveguide with an island structure,” *J Physical Soc Japan*, vol. 89, no. 2, 2020, doi: 10.7566/JPSJ.89.024402.

[61] J. Helszajn and M. McKay, “0°, 90°, and 180° Passive Power Dividers,” *Microwave Polarizers, Power Dividers, Phase Shifters, Circulators, and Switches*, pp. 301–319, Nov. 2018, doi: 10.1002/9781119490104.CH20.